Flexural Capacity of Micropile Threaded Connections

Final Report
December 2025

Principal Investigator: Aaron Gallant

Civil and Environmental Engineering
University of Maine

Authors
Aaron Gallant; Sebastian Montoya-Vargas; William Davids

Sponsored By
Transportation Infrastructure Durability Center

A report from
University of Maine
Department of Civil and Environmental Engineering
5711 Boardman Hall
Orono, Maine 04469

About the Transportation Infrastructure Durability Center

The Transportation Infrastructure Durability Center (TIDC) is the 2018 US DOT Region 1 (New England) University Transportation Center (UTC) located at the University of Maine Advanced Structures and Composites Center. TIDC's research focuses on efforts to improve the durability and extend the life of transportation infrastructure in New England and beyond through an integrated collaboration of universities, state DOTs, and industry. The TIDC is comprised of six New England universities, the University of Maine (lead), the University of Connecticut, the University of Massachusetts Lowell, the University of Rhode Island, the University of Vermont, and Western New England University.

U.S. Department of Transportation (US DOT) Disclaimer

Acknowledgements

Funding for this research is provided by the Transportation Infrastructure Durability Center at the University of Maine under grant 69A3551847101 from the U.S. Department of Transportation's University Transportation Centers Program and the micropile technical committee serving the Association of Drilled Shaft Contractors (ADSC-IAFD). The study was also made possible by the in-kind contributions provided by NUCOR Skyline, OCI Division, GMS Piling Solutions, and Maine Drilling and Blasting. The authors would finally like to thank Laura Krusinski, Garrett Gustafson, and Dale Peabody from the Maine Department of Transportation, whose financial support in assessment of micropile-supported integral abutment bridges helped seed many of the ideas carried out in this study.

Technical Report Documentation Page

1. Report No.	2. Government Accession No.	3. Recipient Catalog No.
4 Title and Subtitle Flexural Capacity of Micropile Threaded Connections		5 Report Date 6 Performing Organization Code
7. Author(s) Aaron Gallant; Sebastian Montoya-Vargas; William Davids		8 Performing Organization Report No.
9 Performing Organization Name and Address		10 Work Unit No. (TRAIS) 11 Contract or Grant No.
12 Sponsoring Agency Name and Address		13 Type of Report and Period Covered 14 Sponsoring Agency Code

15 Supplementary Notes

16 Abstract

This report investigates the flexural behavior of threaded micropile connections under pure bending and combined axial compression and bending, with emphasis on joint-level kinematics and failure mechanisms that are not explicitly addressed in current design practice. A coordinated program of full-scale four-point bending tests, augmented with high-resolution digital image correlation, was conducted to characterize strain localization, joint seam separation, and governing failure modes. Results from pure bending tests demonstrate that flexural capacity is controlled by localized tensile-driven joint kinematics, with failure occurring through jump-out or rupture depending on joint geometry. Combined loading tests reveal that axial compression can delay joint separation and increase flexural capacity, contrary to conventional axial–flexural interaction assumptions. For the axial load range examined, combined loading increased flexural capacity by an average of approximately 15% relative to pure bending. Building on these observations, a mechanics-based analytical framework was developed to predict joint flexural capacity under combined loading by explicitly accounting for joint kinematics. The proposed approach justified higher flexural capacities—on the order of 20–60% relative to conventional design predictions for the loading conditions investigated—while remaining generally conservative, and provides a more physically consistent basis for evaluating threaded micropile connections subjected to bending and combined loading.

17 Key Words	18 Distribution Statement No restrictions. This document is available to the public through		
19 Security Classification (of this report) Unclassified	20 Security Classification (of this page) Unclassified	21 No. of pages	22 Price

Form DOT F 1700.7 (8-72)

Contents

Abstract

This report investigates the flexural behavior of threaded micropile connections under pure bending and combined axial compression and bending, with emphasis on joint-level kinematics and failure mechanisms that are not explicitly addressed in current design practice. A coordinated program of full-scale four-point bending tests, augmented with high-resolution digital image correlation, was conducted to characterize strain localization, joint seam separation, and governing failure modes. Results from pure bending tests demonstrate that flexural capacity is controlled by localized tensile-driven joint kinematics, with failure occurring through jump-out or rupture depending on joint geometry. Combined loading tests reveal that axial compression can delay joint separation and increase flexural capacity, contrary to conventional axial–flexural interaction assumptions. For the axial load range examined, combined loading increased flexural capacity by an average of approximately 15% relative to pure bending. Building on these observations, a mechanics-based analytical framework was developed to predict joint flexural capacity under combined loading by explicitly accounting for joint kinematics. The proposed approach justified higher flexural capacities—on the order of 20–60% relative to conventional design predictions for the loading conditions investigated—while remaining generally conservative, and provides a more physically consistent basis for evaluating threaded micropile connections subjected to bending and combined loading.

Chapter 1: Introduction and Background

1.1 Project Motivation

Micropiles are widely used in foundation engineering for new construction, rehabilitation, and retrofit applications due to their versatility, high load capacity, and constructability in constrained environments. Many of these applications—including bridge foundations, offshore and waterfront structures, transmission towers, wind turbine foundations, and integral abutment bridges—subject micropiles to significant bending demands in combination with axial loading. In such systems, threaded casing connections are commonly used to facilitate installation and load transfer; however, these connections introduce a structural discontinuity that can govern flexural performance.

Current design practice for micropiles under combined axial load and bending relies on interaction equations developed for continuous steel members and codified in standards such as AASHTO and AISC (AASHTO, 2017; AISC, 2023). At threaded joints, these approaches are typically coupled with the "50%-Rule," in which the wall thickness at the joint is reduced by 50% when computing flexural capacity to account for the presence of threads (Sabatini et al., 2005). While this simplified approach is convenient for design, it lacks a clear mechanical basis and does not explicitly account for the kinematics and failure mechanisms unique to threaded connections. Although often regarded as conservative, limited publicly available experimental evidence exists to substantiate this assumption across the range of joint geometries and loading conditions encountered in practice.

The motivation for this project is therefore to improve the fundamental understanding of flexural behavior at threaded micropile joints and to evaluate the influence of combined axial and bending loads from a mechanics-based perspective. In particular, recent observations suggest that flexural failure at threaded connections is governed by tensile-controlled joint kinematics rather than by uniform section yielding, raising the possibility that axial compression may delay joint separation and alter the flexural response in ways not captured by conventional interaction-based design assumptions. By integrating full-scale experimental testing with detailed strain and displacement measurements, this study directly examines how joint kinematics evolve under pure bending and combined loading conditions. The resulting experimental insights form the basis for the analytical developments presented in subsequent chapters.

Ultimately, the work aims to support the development of more reliable and less ambiguous design approaches for micropile joints subjected to pure bending and combined loading conditions, while also making high-quality experimental data publicly available to inform engineering practice.

1.2 Background

Threaded casing connections are an integral component of micropile construction, enabling modular installation and load transfer. While micropiles are routinely designed to resist significant bending demands in applications such as slope stabilization (e.g., Sun et al., 2013; Xiang et al., 2015), excavation support (e.g., Yang et al., 2024), integral abutment bridges (e.g., Pétursson et al., 2011), offshore structures (e.g., Cerfontaine et al., 2023; Thusyanthan et al., 2021), and wind

turbine foundations (Matos et al., 2016), the structural behavior of threaded joints under flexure has historically received less attention than axial performance. As a result, design guidance has largely evolved from simplified assumptions intended to ensure conservatism, rather than from mechanics-based characterization of joint behavior.

Current design practice for micropiles subjected to combined axial load and bending generally follows interaction frameworks developed for continuous steel members, as codified in AASHTO and AISC specifications (AASHTO, 2017; AISC, 2023). At threaded connections, these approaches are commonly coupled with the so-called 50%-Rule, in which the effective wall thickness at the joint is reduced by half when computing flexural capacity (Sabatini et al., 2005). This assumption, which reduces the nominal moment capacity at joints by approximately 40–50%, is attractive due to its simplicity but implicitly treats the threaded region as a uniformly weakened continuous section. In doing so, it does not explicitly account for the kinematics, stress redistribution, or failure mechanisms unique to pin–box threaded connections.

Experimental investigations conducted over the past several decades have demonstrated that threaded micropile joints exhibit distinct failure mechanisms that deviate from classical section yielding assumptions. Early tension tests by Clinedinst (1965) identified two dominant failure modes—jump-out and rupture. The limited experimental studies investigating the bending capacity of micropiles have shown that flexural failures are likewise localized at threaded connections and that these failure modes also govern bending behavior (Musselman et al., 2007; de la Fuente et al., 2009; Babalola et al., 2011; Anderson & Babalola, 2011; Zanuy et al., 2012; Montoya-Vargas et al. 2022). These studies further indicated that the ratio of joint flexural capacity to the yield capacity of an intact casing can vary widely, ranging from approximately 40% to 90%, suggesting that the 50%-Rule may be overly conservative in many cases and unconservative in others depending on joint details.

Despite these insights, publicly available full-scale experimental data capturing joint-level kinematics, strain development, and failure mechanisms remain limited. Most prior studies relied on discrete strain measurements or global load–deflection responses, which are insufficient to fully characterize the complex interactions governing joint behavior under pure bending. Moreover, no experimental studies have explicitly investigated the combined effects of axial compression and bending on threaded micropile joints. Consequently, designers often lack the experimental evidence needed to evaluate whether conventional interaction-based design assumptions are conservative, unconservative, or inconsistent across joint geometries and loading regimes.

This gap in background knowledge motivates the need for systematic full-scale testing with high-resolution measurements capable of resolving joint-level kinematics and informing mechanics-based predictive models. Addressing these limitations provides the foundation for the experimental program and analytical developments presented in the subsequent chapters of this report, with particular emphasis on understanding how combined axial compression and bending influence joint behavior and flexural capacity.

1.3 Research Objectives and Report Overview

The primary objective of this research is to improve understanding of the flexural behavior of threaded micropile joints and to evaluate how combined axial compression and bending influence flexural capacity. In particular, the study seeks to move beyond simplified section-based design assumptions by directly investigating the joint-level kinematics—such as gap opening, box-end dilation, and thread load transfer—that govern flexural response and capacity. Through this effort, the research aims to clarify the limitations of existing design approaches and to establish a more physically consistent basis for evaluating threaded micropile connections subjected to bending and combined loading.

To achieve these objectives, a coordinated experimental and analytical program was conducted. Full-scale four-point bending tests were performed on grouted micropile specimens with threaded casing connections, including tests under pure bending and tests incorporating controlled axial compressive loads. High-resolution digital image correlation and conventional instrumentation were used to capture global response as well as localized strain and displacement fields at the threaded joints, enabling direct observation of failure mechanisms and stiffness transitions. Building on the experimental findings, an analytical framework was developed to relate flexural capacity to joint kinematics and to quantify the influence of axial compression within an interaction-based design context.

This report is organized as follows. Chapter 2 describes the experimental program conducted under pure bending, including specimen details, instrumentation, observed joint kinematics, and governing failure modes. Chapter 3 presents the augmented experimental program examining combined axial compression and bending, with emphasis on the influence of axial load on stiffness evolution, gap opening, and flexural capacity. Chapter 4 introduces a mechanics-based analytical framework for predicting flexural capacity under combined loading and evaluates its performance relative to conventional design approaches. Finally, Chapter 5 summarizes the principal findings of the study, discusses design implications, and outlines recommendations for future research.

Chapter 2: Flexural Capacity and Failure Modes under Pure Bending

The objective of this study was to improve understanding of the flexural behavior of micropile threaded connections subjected to bending, with particular emphasis on failure mechanisms that are not adequately represented by current design practice. Existing approaches commonly idealize micropiles as continuous members by assuming a nominal 50 % reduction in wall thickness at threaded joints when estimating flexural capacity (Sabatini et al., 2005; AASHTO, 2017). While this assumption has been widely adopted due to its simplicity, it lacks a clear mechanical basis and does not explicitly account for the joint-level kinematics that govern failure modes and ultimate strength. Previous experimental studies have shown that threaded connections can fail through mechanisms that are fundamentally different from those assumed in continuous-section behavior, including jump-out and rupture driven by localized deformation at the joint (Zanuy et al., 2012; Musselman et al., 2007). To address this ambiguity, the present study was designed to systematically evaluate how casing geometry and thread characteristics—specifically casing diameter, wall thickness, thread engagement length, thread shape, and wall taper—influence both the flexural capacity and the governing failure mode of threaded micropile connections.

A comprehensive experimental program of four-point bending tests was conducted to isolate pure bending behavior at the threaded joint and to directly observe the transition between the two primary failure modes, jump-out and rupture, as identified in prior work (Zanuy et al., 2012; Montoya-Vargas et al., 2023). High-resolution displacement and strain fields were measured using three-dimensional Digital Image Correlation (DIC), an approach that has proven effective for capturing localized deformation and strain concentrations in steel connections (ZEISS, 2023). Application of DIC enabled direct measurement of joint-level kinematics, including axial and hoop strain development, box dilation, and relative pin–box displacements, providing insight into the mechanisms by which thread slip, wall deformation, and localized plastification control failure.

By generating high-fidelity experimental data across a broad range of casing diameters and thread geometries representative of practice, the study sought to clarify why the flexural strength of threaded micropile connections can vary widely relative to conventional design predictions. Experimental evidence from previous studies has indicated that simplified section-reduction approaches often lead to conservative and highly scattered strength estimates (Zanuy et al., 2012; Montoya-Vargas et al., 2025a), but the underlying causes of this variability have remained poorly understood. The ultimate objective of this work is therefore to establish a mechanistic foundation for evaluating micropile joint behavior in bending that could eventually support the development of more physically consistent and reliable approaches for predicting flexural capacity than those afforded by simplified effective wall-thickness assumptions currently used in practice.

2.1 Materials and Methods

Test Description

Four point bending tests were performed on 31 micropiles with a free length of 2.75 m to evaluate the flexural response of threaded connections under controlled bending conditions. The resulting span-to-diameter ratios, ranging from approximately 11 to 15, were selected to ensure that a near-

pure bending state developed at the threaded joint. In each specimen, the joint was located at mid-span, and loads were applied symmetrically on either side of the connection to minimize shear forces and local stress concentrations (Figure 1a and Figure 1b). The load points were positioned 560 mm from the joint seam—approximately two to 3.5 casing diameters—to limit localized effects in accordance with Saint-Venant's principle.

The specimens were simply supported using fixtures that allowed free rotation while providing minimal resistance to horizontal movement, as shown schematically and in the test setup photographs in Figure 1. Concrete bearing blocks, cross-laminated timber panels, and a steel plate were used to elevate the specimens and provide clearance from the strong floor (Figure 1c). All tests were conducted using a load frame with a maximum capacity of 2000 kN, and loading was applied under displacement control at a constant rate of 6 mm/min until failure of the threaded connection occurred.

Although the testing configuration does not replicate all field loading conditions experienced by micropiles, it was intentionally selected to isolate bending-induced behavior at the joint and to enable clear interpretation of joint-level kinematics. The authors note that the results are most applicable to cases where the threaded connection is sufficiently distant from supports and concentrated loads.

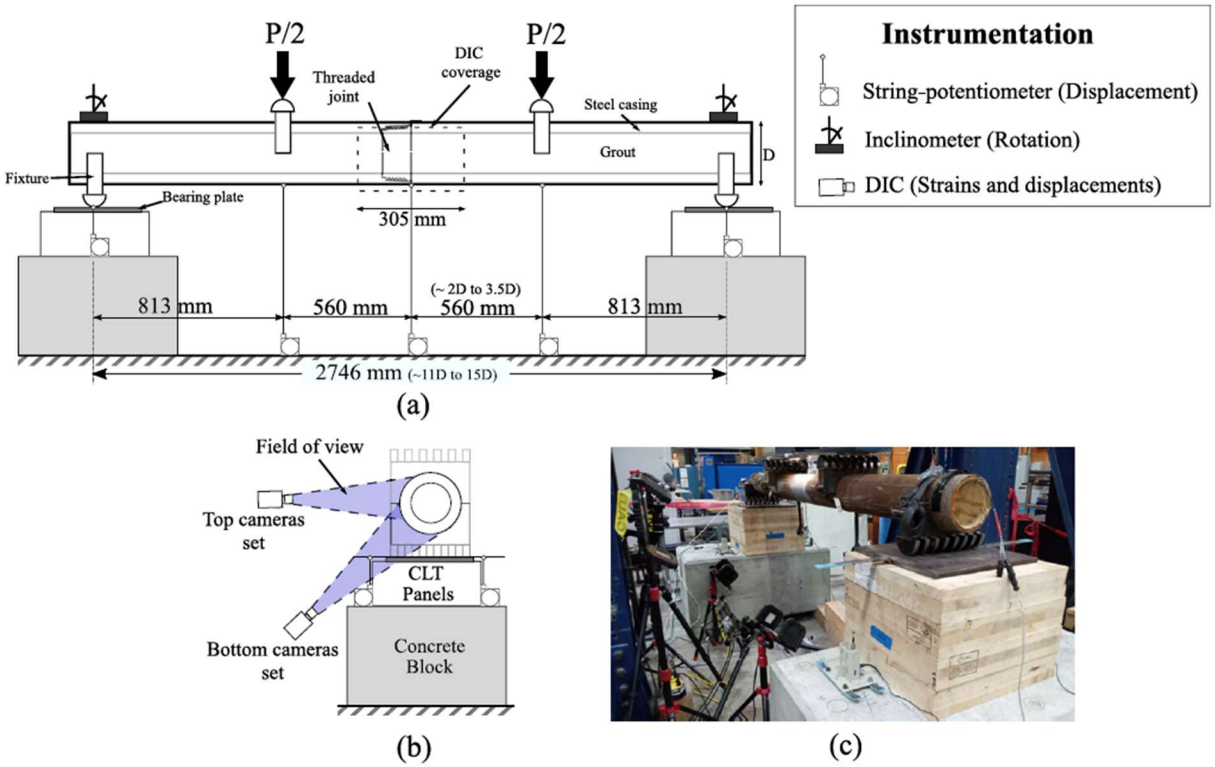

Figure 1. Four-point bending test typical configuration (NTS). Schematic setup: (a) front view and (b) lateral view; and (c) actual setup (after Montoya-Vargas et al. 2025a).

Specimen Construction

Specimen construction was performed above ground and attempted to mimic important aspects of vertical micropile installation procedures that might influence bending capacity. Each specimen consisted of two 1.5 m long steel casing segments that were first threaded together by hand using grease to lubricate the threads. After hand tightening, the connections were torqued using a hydraulic wrench to simulate typical field "make-up" torque conditions applied during drilling operations. Applied torques ranged from approximately 7 to 15 kNm, with the torque level for each specimen. Figure 2a shows the application of make-up torque during assembly.

Following threading and torquing, the casings were positioned vertically and filled with a cement grout (see Figure 2b) having a water–cement ratio of approximately 0.3. Grouting was performed until each casing was filled, replicating standard micropile construction practice. A total of four grout batches were required to fabricate all specimens. From each batch, six 50 mm cube specimens were cast and later tested to determine grout compressive strength, which is reported in Table 1. This construction procedure ensured consistency among specimens while maintaining realistic joint conditions, material properties, and installation effects representative of field-installed micropiles.

(a) (b)

Figure 2. Micropile assemblage and construction: (a) Make-up torque procedure; and (b) Gravity grouting operation (after Montoya-Vargas et al. 2025b).

Micropile Thread Types

Three distinct threaded connection types were selected to represent commonly used and mechanically contrasting designs, as illustrated schematically in Figure 3. Thread type A corresponds to a typical API-like connection with V-shaped threads, a flat crest, rounded root, and a tapered wall (Figure 3a). Thread type B retains the same V-shaped thread geometry but eliminates the wall taper, resulting in a uniform wall thickness through the joint region (Figure 3b). Thread type C consists of a straight-walled connection with square (box) threads and vertical thread faces, a geometry intended to inhibit relative slip between the pin and box ends (Figure 3c).

Across these thread types, four nominal casing outer diameters—178, 194, 244, and 346 mm—were considered in order to span a broad range of practical micropile sizes. Key geometric parameters defining each joint configuration include the intact casing wall thickness (t), pin- and box-end wall thicknesses (t_1 and t_2), thread engagement length (L), nominal shoulder-to-shoulder distance (L'), thread height, and wall taper (α), all of which are defined in Figure 3. These parameters were systematically varied to isolate the effects of thread length, wall thickness, and thread shape on strain development, joint kinematics, failure mode, and flexural capacity.

Material properties were verified for each batch of casing through coupon testing to determine yield stress and ultimate tensile strength, ensuring consistency across specimens. The full matrix of tested specimens—including thread type, casing diameter (D), geometric details, grout strength (f_g), steel yield and ultimate strengths (f_y and f_u), applied make-up torque (T), and corresponding test identifiers—is summarized in Table 1. By varying thread type and casing size across this test matrix, the experimental program was structured to directly assess how threaded length, wall thickness, and thread geometry govern strain distributions and failure mechanisms at micropile threaded connections under bending.

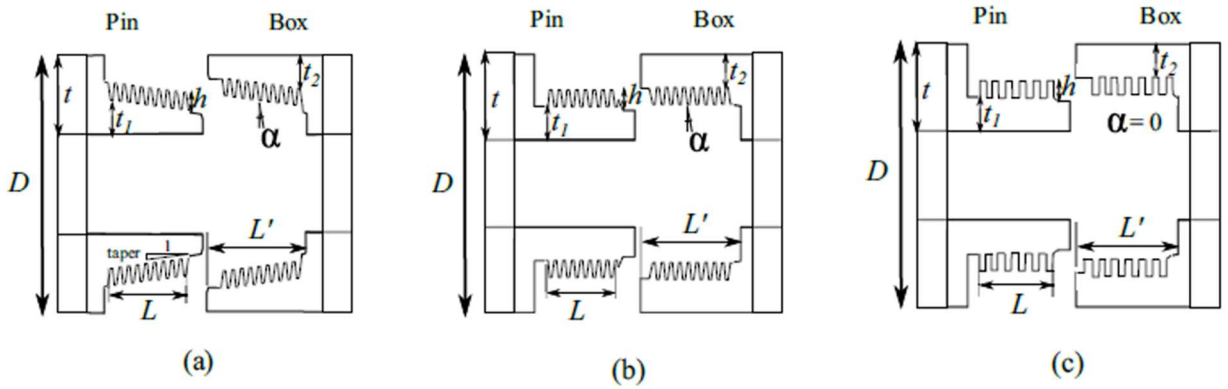

Figure 3. Schematic representation of thread types (NTS): (a) type A with V-threads and tapered walls; (b) type B with V-threads and no wall taper; and (c) type C with square threads and no wall taper (after Montoya-Vargas et al. 2025a).

Table 1. Summary of tested specimens and thread and casing details (after Montoya-Vargas et al. 2025a)

Thread type	D (mm)	t (mm)	L' (mm)	L (mm)	h (mm)	Wall taper (mm/mm)	t_1 (mm)	t_2 (mm)	f_g[a] (MPa)	f_y[b] (MPa)	f_u[b] (MPa)	T[c] (kNm)	Test ID
A	194	12.7	51	25	2.3	0.0625	5.3	5.3	47	915	986	12	1–3
A	194	12.7	64	38	2.3	0.0625	5.6	5.6	47	956	1018	11	4–6
A	194	12.7	76	57	2.3	0.0625	5.9	6.1	69	931	1014	11	7–9
A	244	13.8	64	38	2.3	0.0625	5.8	5.3	55	932	989	12	10–12
A	244	13.8	76	57	2.3	0.0625	6.5	6.1	55	932	989	11	13 and 14
A	346	15.9	89	64	2.2	0.0521	7.1	7.4	51	1007	1103	10	15
A	346	15.9	127	102	2.2	0.0521	7.8	8.1	51	1016	1110	10	16–18
B	178	11.5	51	32	2.6	0	3.7	3.7	55	896	971	9	19–21
B	244	13.8	51	32	2.6	0	5.1	5.1	69	700	802	14	22–25
B	244	13.8	76	51	2.6	0	5.1	5.1	69	710	803	12	26 and 27
C	244	13.8	51	32	3	0	5.1	5.1	47	720	829	13	28–31

[a] Average 50 mm-Cube compressive strength. Actual values for each test might vary by up to ±7 MPa
[b] Average value reported. Actual values for each test might vary by up to ±5 %
[c] Average value reported. Actual values for each test might vary by up to ±5 kNm

Instrumentation and Data Processing

Instrumentation and data-processing procedures used were intended to quantify both global specimen response and localized joint kinematics during testing. Global vertical displacements were measured at five locations along each specimen—including the loading points, mid-span, and supports—using string potentiometers with an accuracy of 0.25 mm. Specimen end rotations were measured using inclinometers with a resolution of 0.1° (see Figure 1). Measured deflections included contributions from deformation of the wood-block support system; therefore, rigid-body motions associated with support compliance were removed from the recorded data. Support deflections were generally less than 3.8 mm, corresponding to approximately 10% of the total mid-span deflection, and differential support movements were sufficiently small such that their influence on the bending response was considered negligible.

Local displacement and strain fields at the threaded connection were measured on the exterior surface of the box-end using three-dimensional digital image correlation (DIC) techniques. A speckle pattern was placed on the exterior surface of the box-end of the casing in the vicinity of the joint, as illustrated in Figure 4. The DIC system employed stereo-vision principles to resolve full-field displacement components in the global x-, y-, and z-directions, enabling simultaneous measurement of axial, hoop, and out-of-plane deformations at the joint. The experimental configuration consisted of two independent stereo camera pairs, each comprising two 2-megapixel cameras equipped with 16 mm focal-length lenses. Within each stereo pair, the cameras were positioned 41 cm apart, while the camera systems were placed approximately 88.9 cm from the micropile joint. This arrangement provided a measurement field approximately 305 mm wide by 229 mm high, with overlapping regions along the top and bottom of the casing circumference (Figure 1b). As a result, displacement and strain data were captured over approximately 140 degrees of the micropile perimeter, corresponding to roughly three-quarters of the cross-section depth, while ensuring complete coverage of the bottom half of the casing—the tension side of the joint where failure was anticipated to initiate.

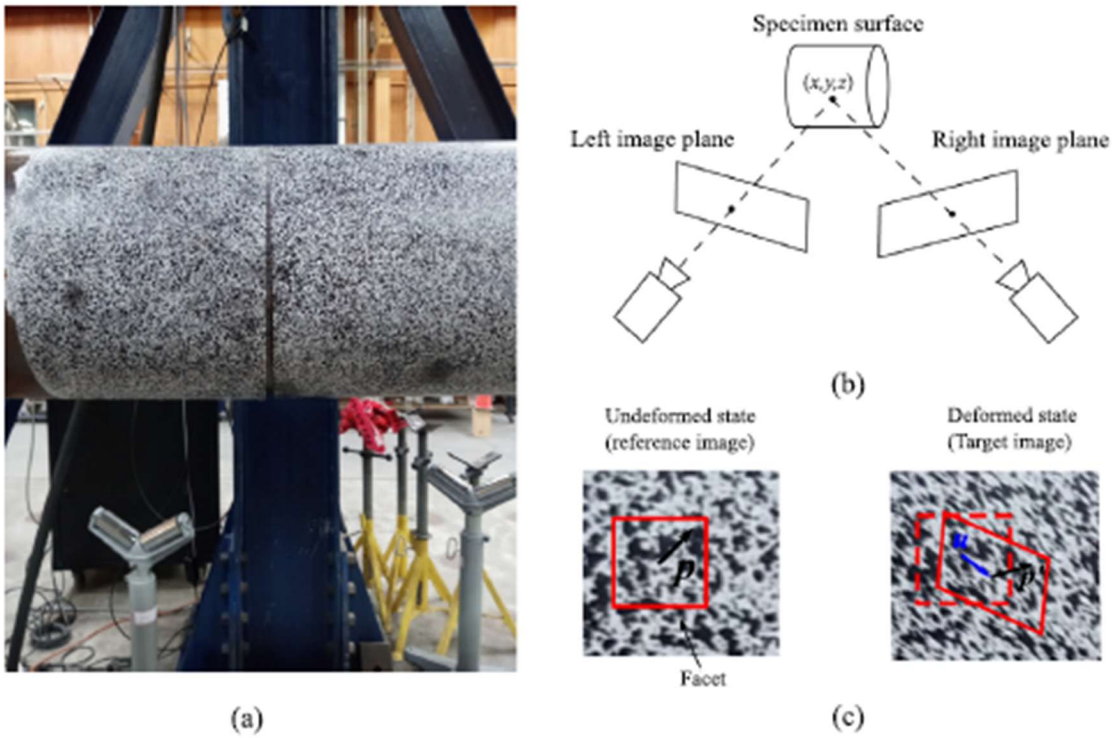

Figure 4. DIC working principle: (a) Example of speckle pattern on the surface of the threaded joint; (b) Projection of point with coordinates (x, y, z) into the image plane of each camera; and (c) Evolution of a 'Facet' element from the undeformed (reference) configuration to the deformed (target) configuration.

Prior to testing, noise characteristics of the DIC system were evaluated using static images acquired for each specimen. Analysis of these images showed that raw strain measurements exhibited approximately Gaussian noise distributions with zero mean and standard deviations on the order of 400 με for axial strains and 600 με for hoop strains (e.g. Figure 5). To improve signal fidelity, a spatial median filter was applied to the raw strain fields, reducing the standard deviation of noise to approximately 150 με for axial strains and 200 με for hoop strains. Following filtering, approximately 90 % of the noise-induced strain fluctuations were confined within ±256 με. All strain data presented and interpreted in the study correspond to these filtered measurements.

It is important to note that DIC-based deformation measurements inherently rely on the assumption of material continuity across the imaged surface. As a consequence, displacement and strain values calculated directly at the joint seam—where physical discontinuities exist—are unreliable. For this reason, data in the immediate vicinity of the pin shoulder and joint interface were excluded from analysis. The omission of these measurements reflects a methodological limitation of the DIC technique rather than evidence of joint separation or loss of contact between the pin and box ends during testing.

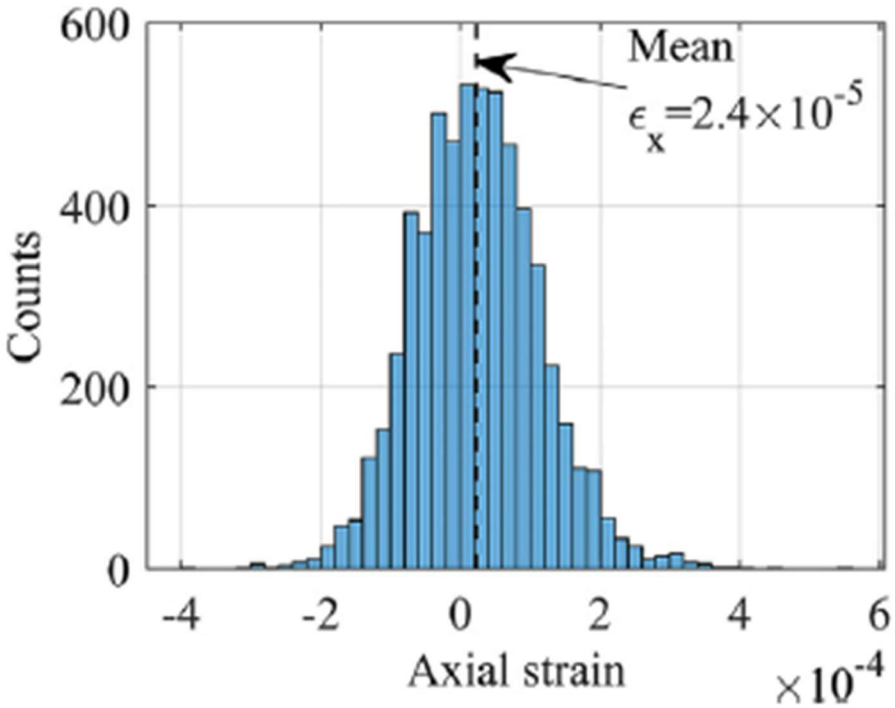

Figure 5. Histogram of axial strain measurements for static images of Test 01 (base noise).

Digital Image Correlation (DIC) images were processed using *GOM Correlate Professional v2019* (Zeiss 2023) to compute full-field displacement and strain measurements at the threaded joint. Because micropiles are cylindrical structural elements, deformations and displacements were interpreted with reference to the cylindrical coordinate system (x, r, θ)shown in Figure 6a, where $x$denotes the axial direction of the micropile, $r$the radial direction, and $\theta$the circumferential direction. Strain calculations were initially performed in the material (local) coordinate system intrinsic to the DIC formulation, consisting of directions $x'$and y'tangent to the surface of the casing and z'normal to the tangent plane (Figure 6b).

Because joint-level deformations were small relative to the global mid-span deflections of the specimen, DIC-derived displacement fields were subjected to rigid-body motion compensation. This was accomplished by referencing relative displacements to the center of mass of the imaged region, thereby removing contributions from overall specimen translation and rotation. Under the assumption of small local deformations, the material coordinate system $(x', y', z')$was taken to be approximately coincident with the cylindrical coordinate system (x, θ, r). This approximation allowed direct interpretation of the DIC strain components as axial strain $\varepsilon_x = \varepsilon_{x'}$, hoop strain $\varepsilon_\theta = \varepsilon_{y'}$, radial strain $\varepsilon_r = \varepsilon_{z'}$, and axial–hoop shear strain $\varepsilon_{x\theta} = \varepsilon_{x'y'}$.

Using these strain components, material deformations were described in terms of axial, hoop, shear, and radial strain fields without imposing assumptions regarding elastic behavior. To evaluate the extent of inelastic deformation and the onset of yielding within the joint region, the equivalent Von Mises strain, ε_{VM}, was computed from the principal strains according to

$$\varepsilon_{vm} = \sqrt{\frac{2}{3}[(\varepsilon_1 - \varepsilon_2)^2 + (\varepsilon_2 - \varepsilon_3)^2 + (\varepsilon_1 - \varepsilon_3)^2]} \quad (1)$$

where the principal strains ε_1, ε_2, and ε_3 are given by

$$\varepsilon_1 = \frac{\varepsilon'_x + \varepsilon'_y}{2} + \sqrt{\left(\frac{\varepsilon'_x - \varepsilon'_y}{2}\right)^2 + \varepsilon^2_{x'y'}} \quad (2a)$$

$$\varepsilon_2 = \frac{\varepsilon'_x + \varepsilon'_y}{2} - \sqrt{\left(\frac{\varepsilon'_x - \varepsilon'_y}{2}\right)^2 + \varepsilon^2_{x'y'}} \quad (2b)$$

$$\varepsilon_3 = -(\varepsilon_1 + \varepsilon_2) \quad (2c)$$

These expressions implicitly assume negligible shear deformation in the z'-direction and no net volumetric strain. Importantly, the strain calculations performed by *GOM Correlate* do not inherently impose restrictions on displacement magnitude or material response (Zeiss 2023). This processing framework enabled consistent interpretation of localized axial, hoop, and combined strain development at the threaded connection and formed the basis for subsequent analysis of joint kinematics, plastic deformation, and failure mechanisms.

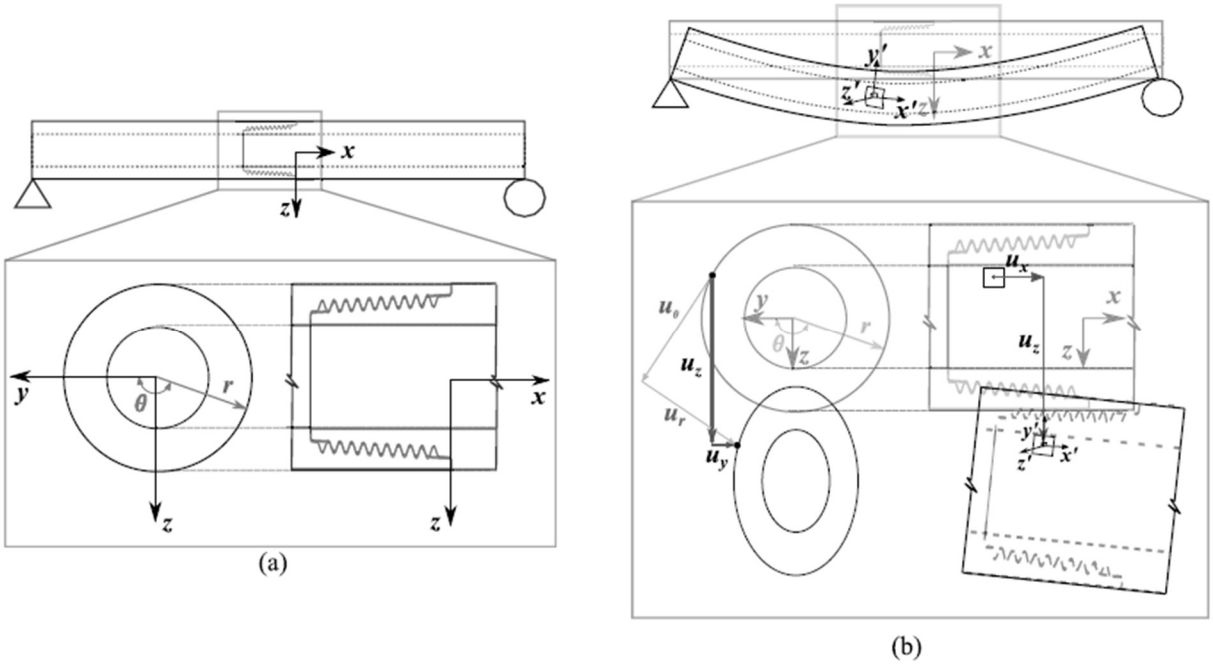

Figure 6. DIC coordinate system: (a) Global coordinate system x-y-z; and (b) local coordinate system x'-y'-z' (Montoya-Vargas et al. 2025b).

2.2 Test Results and Thread Joint Kinematics

The flexural strength and ultimate bending moment capacity of micropile threaded joints were observed to vary significantly with casing diameter, thread engagement length, and thread type, as summarized in Table 2 and visualized in Figure 7. These results highlight the sensitivity of joint behavior to geometric and connection details. In contrast, current design practice typically estimates the flexural capacity at threaded connections by assuming that the effective wall thickness of the intact casing section is reduced by 50 % at the joint. The corresponding predicted moment capacity, denoted herein as M_{50}, is expressed using the notation defined in this study and represents a simplified design approximation as,

$$M_{50} = \frac{\pi[(D-t)^4-(D-2t)^4]}{32(D-t)} f_y \tag{3}$$

Comparison of experimentally measured capacities with predictions based on the 50 % rule shows that this approach systematically underestimates joint strength across the tested specimens, irrespective of the governing failure mode, as illustrated in Figure 7. Implicit in the M_{50} formulation is the assumption that joint failure in bending is controlled by yielding of the pin-end section. However, the experimental results demonstrate that this assumption is not universally valid, and to the authors' knowledge, there is limited publicly available experimental evidence to substantiate its general applicability for design purposes.

Given these discrepancies, the subsequent sections focus on examining joint-level kinematics that led to reductions in stiffness and strength at threaded connections. Particular attention is given to the deformation mechanisms that govern the transition between failure modes and their influence on the flexural capacity of micropiles. Through this analysis, the study seeks to establish a clearer mechanistic understanding of joint behavior in bending, thereby providing a more rational basis for evaluating and improving current design assumptions.

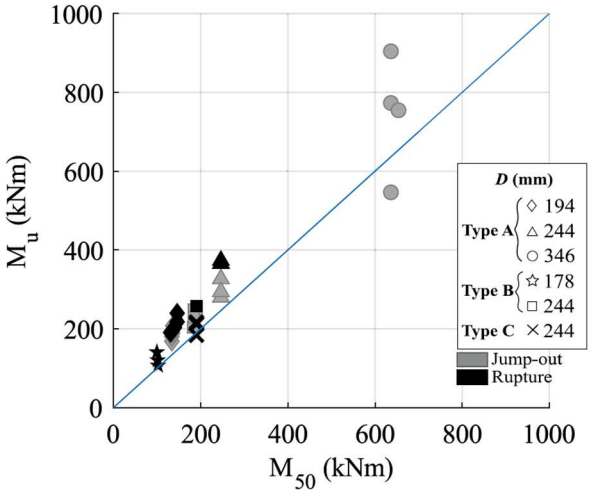

Figure 7. Observed flexural strength (M_u) vs. predicted strength according to the 50 %-Rule (M_{50}) from Montoya-Vargas et al. (2025a)

Table 2. Summary of obtained failure moments and associated failure modes (from Montoya-Vargas et al. 2025a)

Test ID	Thread type	D (mm)	L (mm)	Failure mode *	M_u (kNm)	M_{50} (kNm)
1	A	194	25	JO	168	134
2	A	194	25	JO	180	134
3	A	194	25	JO	189	136
4	A	194	38	R	217	146
5	A	194	38	JO	207	136
6	A	194	38	R	203	140
7	A	194	57	R	239	146
8	A	194	57	JO	191	134
9	A	194	57	R	190	131
10	A	244	38	JO	280	246
11	A	244	38	JO	327	246
12	A	244	38	JO	294	246
13	A	244	57	R	373	246
14	A	244	57	R	366	246
15	A	346	64	JO	773	636
16	A	346	102	JO	546	636
17	A	346	102	JO	904	636
18	A	346	102	JO	755	654
19	B	178	32	R†	120	101
20	B	178	32	R	107	102
21	B	178	32	R†	141	99
22	B	244	32	JO	248	191
23	B	244	32	JO	239	184
24	B	244	32	JO	204	182
25	B	244	32	JO	250	184
26	B	244	51	JO	230	184
27	B	244	51	R	258	191
28	C	244	32	R	217	190
29	C	244	32	R	212	190
30	C	244	32	R	184	190
31	C	244	32	R	212	190

* JO = Jump-out; R = Rupture at the pin-end; R†: Rupture at the box-end

Threaded Joint Kinematics

Using experimental techniques and instrumentation previously discussed, the kinematic behavior of threaded micropile joints under bending, and its relationship to stiffness degradation, failure mode, and flexural capacity, are discussed. At the global scale, the tested micropiles exhibited little evidence of yielding prior to failure, with most specimens demonstrating a mildly non-linear response followed by abrupt, brittle failure localized at the threaded connection. Representative bending moment–deflection responses are shown in Figure 8 for two specimens with identical casing diameter ($D = 194$ mm) but different thread engagement lengths ($L = 25$ mm and $L = 57$mm). For reference, the theoretical elastic response of an intact, continuous micropile section is also shown. In general, the measured responses diverged from the theoretical solution once bending moments exceeded approximately 50 kNm, after which the joint response softened relative to an intact section until failure occurred (as expected).

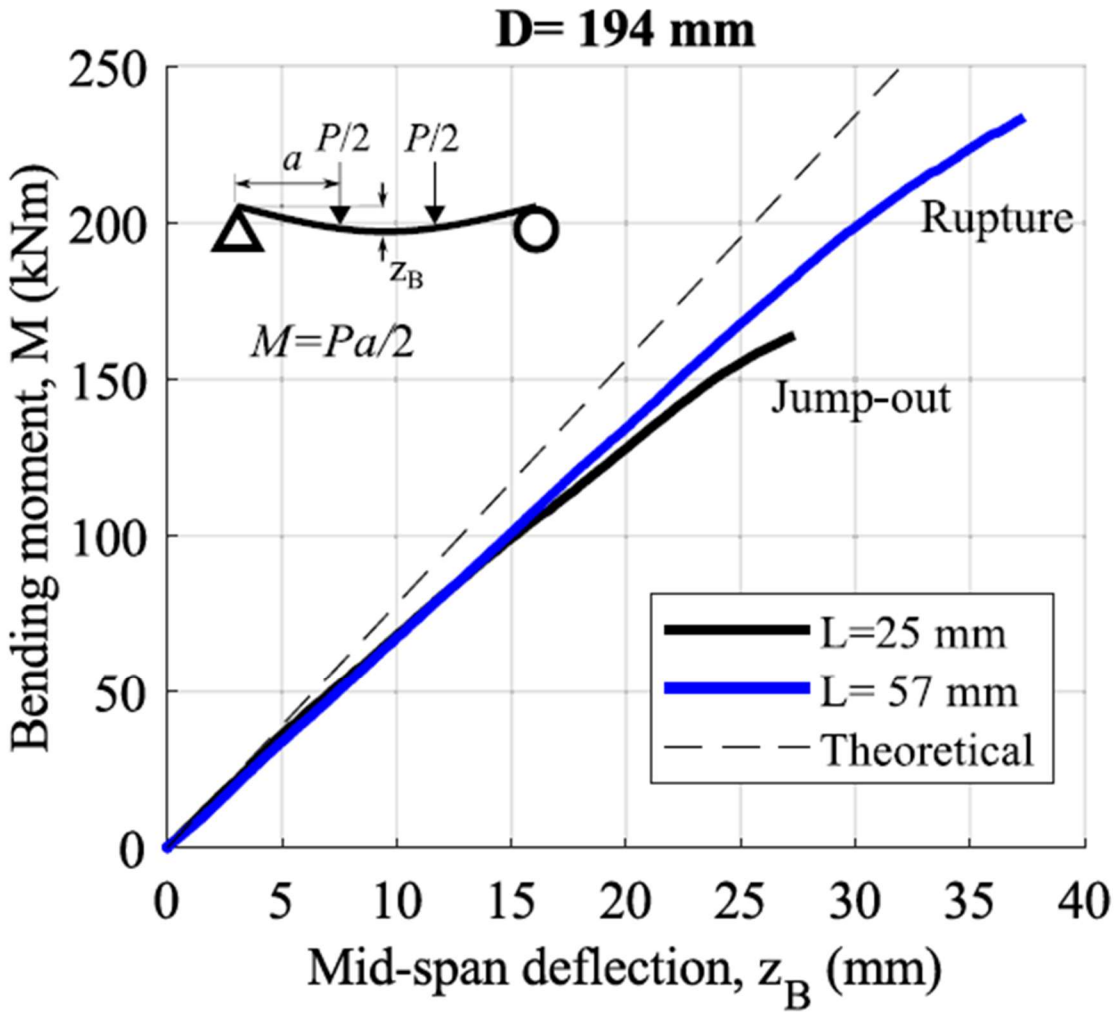

Figure 8. Bending moment vs. deflection curves of representative tests for specimens 1 and 7. (from Montoya-Vargas et al. 2025a)

Although the overall moment–deflection behavior did not clearly distinguish between failure modes, specimens with different thread lengths exhibited markedly different ultimate bending capacities and failure mechanisms. The specimen with shorter threads failed due to jump-out at an ultimate moment of 168 kNm, whereas the specimen with longer threads failed in rupture at an ultimate moment of 239 kNm (Figure 8). Post-test inspection of transverse sections cut through the joints confirmed the failure mode and location. Jump-out failures were characterized by dilation of the box-end and permanent thread slip on the tension side, and loss of thread engagement, while rupture failures were marked by relatively high axial strains (at failure) and tensile cracking, most commonly initiating at the root of the first engaged thread of the pin-end (e.g. see Figure 9). In a small number of cases, rupture occurred at the second or third thread, and only two specimens exhibited rupture at the shoulder of the box-end (specimens 19 and 21 in Table 2).

Because the global response was insufficient to explain the governing failure mechanisms, local joint deformations were examined using DIC. Figure 10 presents displacement and strain fields for two representative specimens at a common bending moment of 168 kNm for specimens that

failed via jump-out and rupture behavior; note that 168 kNm is the moment at which a jump-out failure occurred for the specimen with a shorter thread length. Vertical displacement fields at the bottom fiber (Figure 10a), corrected for rigid-body motion, show that the box-end initially contracts near the shoulder and transitions to dilation closer to the engaged threads, with maximum separation between the box and pin ends occurring near the pin shoulder. This contraction-to-dilation transition induces localized negative curvature at the box shoulder, producing compressive axial strains on the exterior surface of the box-end (Figure 10b).

Axial strains increased significantly in regions where the displacement field reversed from contraction to dilation, indicating transfer of tensile load across the engaged threads. The magnitude of axial strain generally decreased toward the joint seam, consistent with load transfer being concentrated in threads located farther from the outer joint seam where the box-end thread wall is thickest for Type A joints. The most significant distinction between jump-out and rupture behavior was observed in the development of hoop strains (Figure 10c). Specimens that failed by jump-out exhibited substantially larger hoop strains on the tension side of the joint, reflecting dilation of the box-end and associated thread slip attributed to jump-out failures. Greater dilation with the shorter threads is attributed to higher load concentrations on each thread (i.e. fewer number of threads) and smaller thread wall thicknesses (see joint details). Greater dilation also explains the larger negative curvature (Figure 10a) and localized compressive effects (Figure 10b) observed near the box shoulder for jump-out failures.

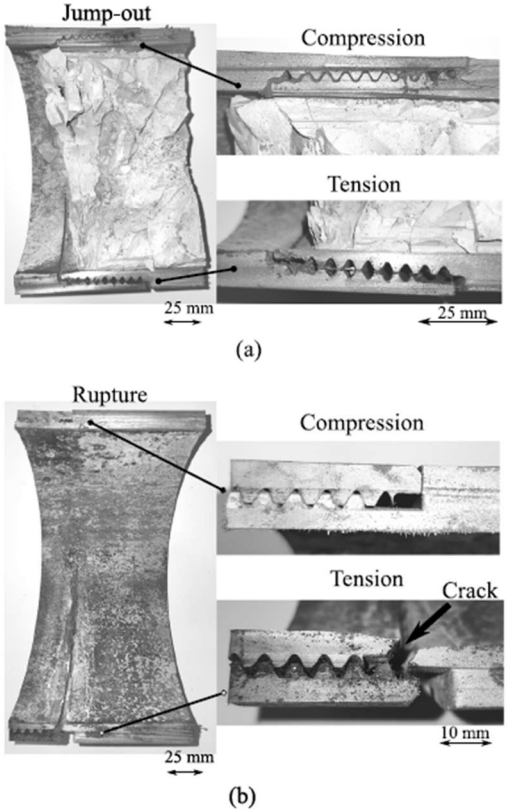

Figure 9. Threaded joint samples failed in: (a) jump-out (specimen 5); and (b) Rupture (specimen 27). (from Montoya-Vargas et al. 2025a).

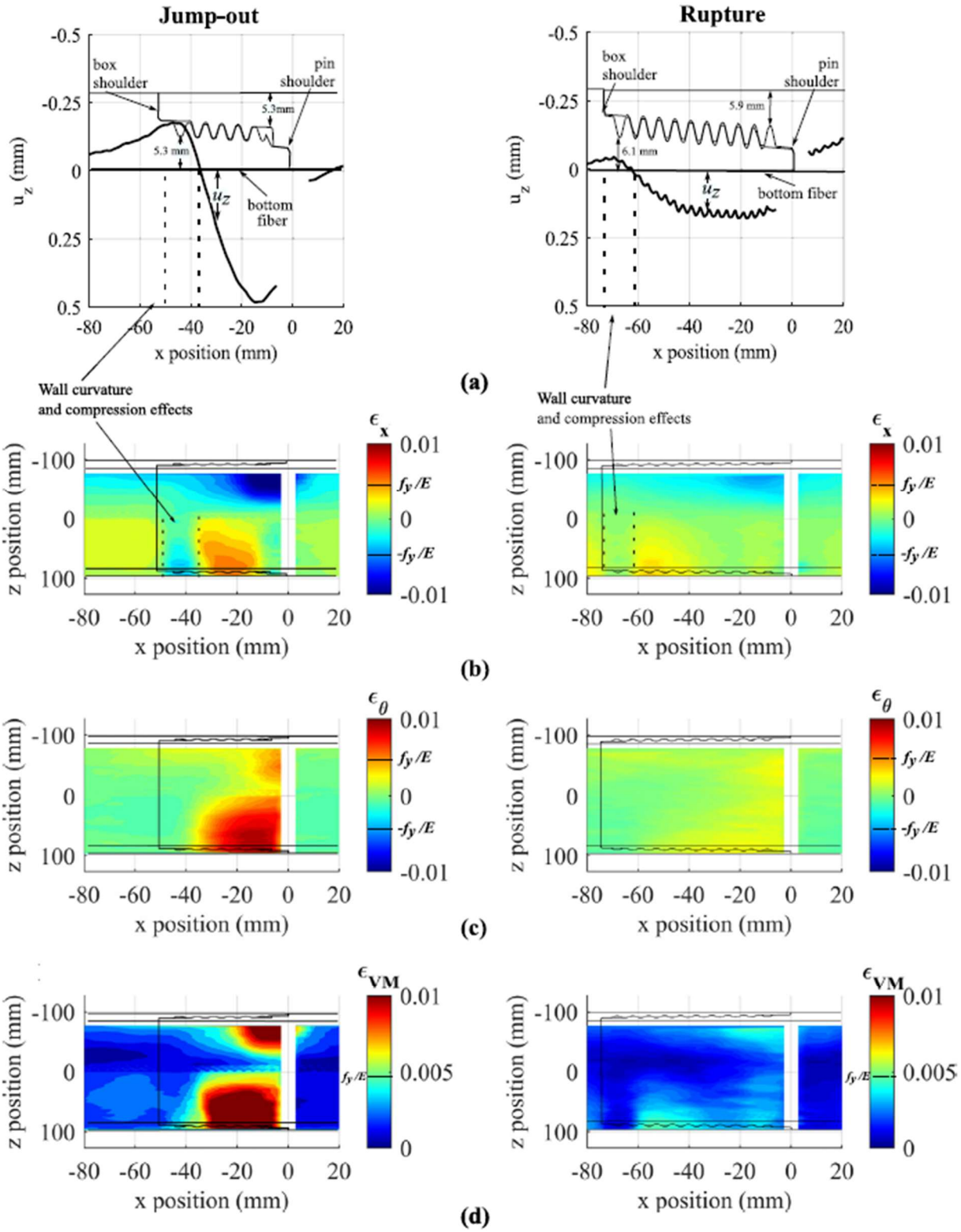

Figure 10. DIC measured strains and displacements for type A threads at M = 168 kNm for specimen with D = 194 mm and threaded lengths L = 25 mm (specimen 1, jump-out, left) and L = 57 mm (specimen 7, rupture, right): (a) vertical displacement, u_z (Thread schematic NTS); (b) axial strain field, ϵ_x ; (c) hoop strain field, ϵ_θ ; and (d) equivalent Von-Mises strain field, ϵ_{vm}. (from Montoya-Vargas et al. 2025a).

Equivalent Von Mises strain fields (Figure 10d) further illustrate differences in deformation mechanisms. Specimens failing by jump-out experienced widespread plastic deformation over a large portion of the joint region, with Von Mises strains exceeding the elastic limit across much of the box-end. In contrast, specimens failing by rupture exhibited a more localized spread of plasticity, even at higher applied moments (e.g. failure), as illustrated in Figure 11 for specimen 7 (i.e. same specimen shown on right side of Figure 10 at lower load level). Comparison of strain fields at failure with those observed for jump-out indicates that rupture is primarily governed by axial strain development (Figure 11), whereas jump-out is strongly influenced by hoop strain accumulation associated with thread slip and box dilation (left side of Figure 10).

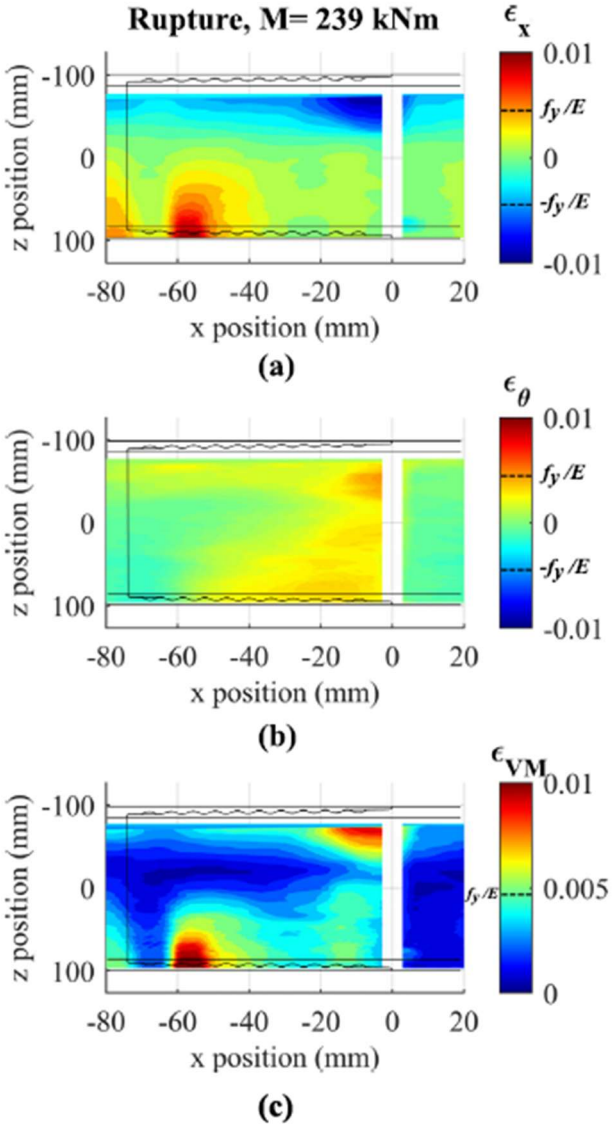

Figure 11. DIC measured strains for specimen 7 with longer threads (D = 194 mm and L = 57 mm) at its failure moment of M = 239 kNm: (a) axial strains; (b) hoop strains; and (c) Von-Mises strain (from Montoya-Vergas et al. 2025a).

Similar kinematic trends were observed for joints with thread types B and C, although the magnitude and distribution of strains differed. Type B threads, which have thinner box walls, exhibited larger hoop strains and greater negative curvature than type A threads of similar length and diameter. Type C threads, which have square thread geometry and vertical contact faces, showed significantly reduced dilation due to inhibited thread slip, although localized flaring of the box-end was still observed.

Joint-level kinematics were further quantified by tracking relative displacements at the pin- and box-ends using DIC data. Relative box dilation (Δu_z) and gap opening (Δu_x) near the joint seam were evaluated as functions of applied bending moment for D = 244 mm specimens where all three thread types were available (Figure 12). Dilation (Δu_z) generally increased steadily with load for rupture specimens, but the rate of dilation increased sharply near failure for jump-out specimens as plastic deformation and hoop strains accumulated. V-shaped threads exhibited greater dilation for thinner walls and shorter engagement lengths, while square threads showed reduced dilation consistent with limited slip expected for this thread shape. Gap opening was influenced primarily by wall thickness and yield strength, with thinner walls and lower yield strength resulting in larger vertical gap openings.

Gap opening at the threaded joint was interpreted as the combined result of relative thread slip and axial deformation of the casing wall (i.e., wall stretching). To evaluate the relative contribution of these two mechanisms, the ratio of gap opening to box dilation, $\Delta u_x/\Delta u_z$, was examined for the different thread configurations, as shown in Figure 12c. Because thread slip occurs along the inclined contact plane of the threads, a joint response governed solely by thread slip—with no contribution from wall stretching—would be expected to satisfy the geometric relationship $\Delta u_x/\Delta u_z = \tan\ \alpha$, where α is the thread face inclination angle. This condition is represented by the dashed line in Figure 12c for $\alpha = 30°$, corresponding to the V-thread geometries used in thread types A and B.

The experimentally observed ratios, however, deviated from this idealized thread-slip condition, indicating that axial deformation of the casing wall contributed to gap opening in addition to thread slip. These deviations reflect the development of axial strain, ε_x, within the joint region and were more pronounced for connections with thinner walls (types B and C). In these cases, wall stretching played a more significant role in increasing gap opening relative to dilation.

Type C threads exhibited the largest values of $\Delta u_x/\Delta u_z$, a response consistent with the relatively small dilation, Δu_z, expected for this thread type. Because type C threads have square profiles with vertical contact faces ($\alpha = 0$), relative thread slip is limited, and gap opening is therefore dominated by axial wall deformation rather than slip-induced dilation. This behavior further supports the interpretation that the ratio $\Delta u_x/\Delta u_z$ provides a useful measure of the competing roles of thread slip and wall stretching in governing joint deformation mechanisms.

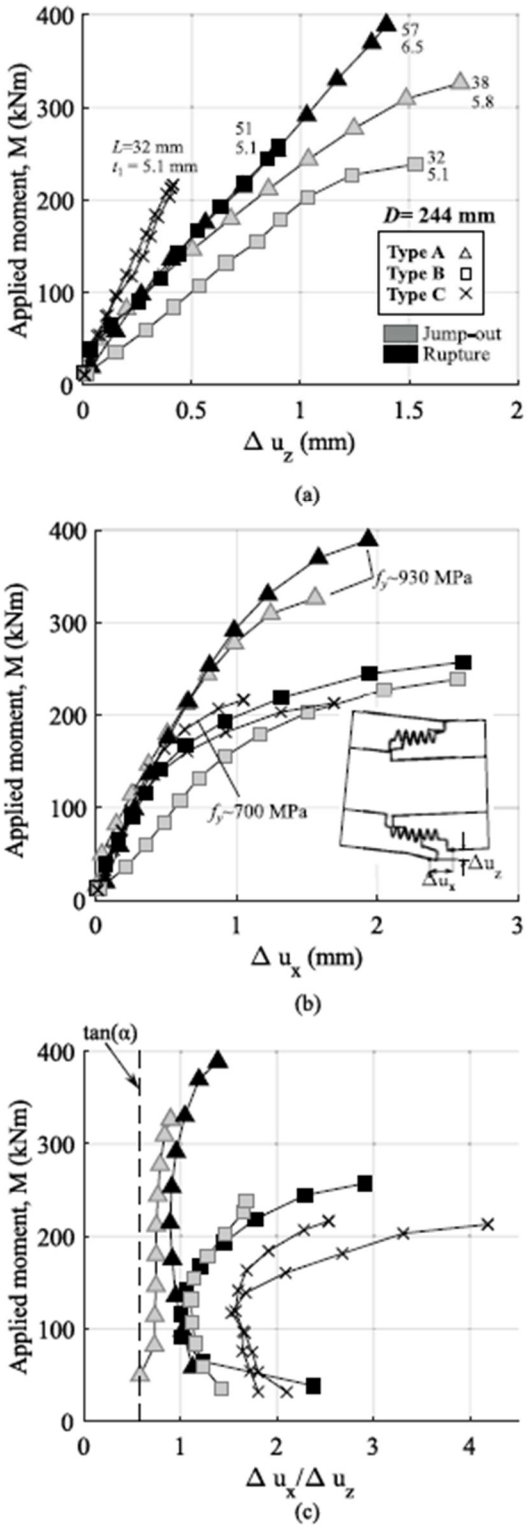

Figure 12. Pin-box relative displacements at the bottom of the joint seam as a function of the applied bending moment fr D = 244 mm specimens: (a) relative box dilation (Δu_z); (b) gap opening (Δu_x); and (c) gap opening to box dilation ratio ($\Delta u_x / \Delta u_z$) compared with tan α that represents thread slip only for v-shaped threads (Types A and B) (from Montoya-Vargas et al. 2025a)

Measured box dilation, Δu_z, remained below approximately 2 mm for most tested specimens, including those that ultimately failed by jump-out. Nevertheless, for jump-out to occur, the relative dilation between the pin and box ends must reach or exceed the thread face contact height, h, which ranged from approximately 2.4 to 3.0 mm depending on thread type. Because DIC images were acquired at a frequency of 1 Hz, the precise instant at which the frictional resistance between threads was exceeded and joint decoupling occurred was not captured. As a result, the DIC measurements obtained at failure represent the joint condition immediately prior to decoupling, and the reported ultimate dilation values are therefore smaller than the actual dilation required to initiate jump-out.

Despite this limitation, clear distinctions between jump-out and rupture behavior are evident in Figure 13, where normalized dilation, $\Delta u_z/h$, is plotted as a function of relative thread engagement length, L/D, for specimens with type A threads. Specimens with shorter thread engagement lengths tended to fail by jump-out with recorded images that suggest normalized dilation levels in the range of approximately $0.7h$ to $0.9h$ were achieved just prior to failure. Rupture failures were more commonly observed in specimens with longer thread engagement lengths, which exhibited normalized dilation values less than approximately $0.65h$. Although all rupture failures occurred for specimens with $L/D > 0.18$, the data does not indicate a distinct threshold value of L/D that uniquely separates jump-out from rupture behavior. Instead, it must be understood that the entire thread detail, including thread wall thickness, associated thread wall taper, and yield strength and ultimate capacity of the steel materials itself need to be optimized together.

One exception to this general trend was observed for a specimen with a casing diameter of $D = 346$ mm and a thread engagement length of $L = 102$mm ($L/D = 0.29$), which nonetheless failed by jump-out. Post-test visual inspection suggested that excessive grease had been applied during torquing, reducing friction at the thread interface and thereby promoting thread slip and jump-out despite the relatively long engagement length.

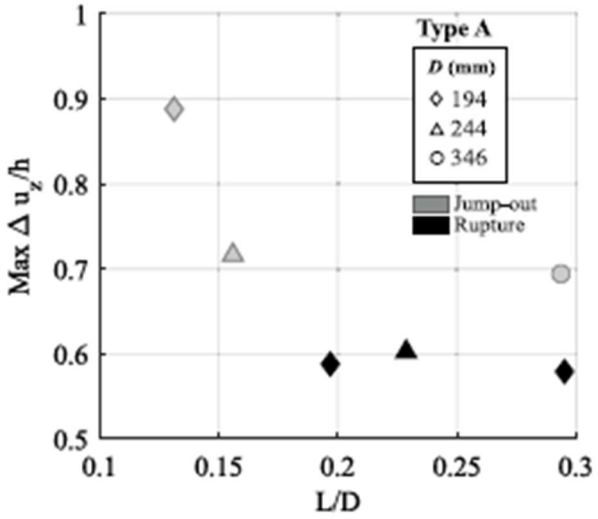

Figure 13. Maximum normalized dilation for different casing diameters and relative joint thread lengths (from Montoya-Vargas et al. 2025a).

Design Implications

The flexural capacity predicted using the 50% wall-thickness rule, M_{50}, does not account for the mechanics governing joint deformation or their dependence on thread geometry and failure mode. Experimental results demonstrate that thread engagement length (L), box-end wall thickness (t_2), and thread geometry—including the thread face inclination angle (α)—strongly influence the development of box dilation and, consequently, the governing failure mode and flexural strength of the joint. These geometric effects directly control the extent of hoop strain and thread slip at the connection; however, they are not explicitly considered in the current design approach.

Comparison between experimentally measured flexural capacities and predictions based on the 50% rule (Figure 7) shows that this method systematically underestimates joint strength for the thread details investigated. For specimens that failed by jump-out, the underestimation was typically on the order of 25%, while for specimens that failed by rupture, discrepancies as large as 39% were observed. As discussed previously, the 50 % rule implicitly assumes that joint failure in bending is governed by yielding of the pin-end section. While rupture failures were indeed observed to initiate predominantly at the pin-end for specimens exhibiting this failure mode, the stress state associated with rupture more closely corresponds to plastification of the cross-section rather than first yield. As a result, flexural capacity is more accurately represented by the plastic moment capacity of the pin-end, M_P,

$$M_p = \frac{f_y}{6}[(D - 2t + 2t_1)^3 - (D - 2t)^3] \tag{4}$$

This expression accounts for the reduced wall thickness at the threaded region while allowing for full section plastification, consistent with the observed rupture behavior. For the limited number of specimens that experienced rupture at the box-end—specifically, two specimens with 178 mm diameter casings and type B threads—a better estimate of flexural capacity is obtained by using the plastic moment capacity of the box section, $M_{P,\mathrm{box}}$, which incorporates the section modulus of the box-end wall as,

$$M_{p,box} = \frac{f_y}{6}[D^3 - (D - 2t_2)^3] \tag{5}$$

To evaluate the performance of different strength prediction approaches, experimentally measured ultimate bending capacities, M_u, were normalized by predictions based on both the 50 % wall-thickness rule, M_{50}, and the plastic moment capacity of the pin-end section, M_P, for all tested specimens, as summarized in Figure 14. For the limited cases in which rupture occurred at the box-end, normalization was performed using the plastic moment capacity of the box section, $M_{P,\mathrm{box}}$, rather than M_P.

The ratio M_u/M_{50}, presented in Figure 14a, demonstrates substantial scatter in the predictions obtained using the 50 % rule. Across the full test dataset, this ratio ranged from a minimum value of approximately 0.86 to a maximum value of 1.64, indicating that the 50% rule both under- and, in some cases, marginally over-predicted the observed capacity. Approximately 35% of the

specimens fell within the range $1 \leq M_u/M_{50} \leq 1.25$, highlighting the limited reliability of this approach and its sensitivity to joint geometry and failure mode.

In contrast, normalization using plastic moment capacity predictions based on M_P or $M_{P,\text{box}}$ resulted in improved agreement with the experimental results. As shown in Figure 14b, approximately 60% of the specimens exhibited normalized capacities within the range $1 \leq M_u/M_P \leq 1.25$, reflecting a substantially tighter clustering of results relative to the 50% rule. The remaining variability in the M_u/M_P ratio was found to correlate with failure mode and joint geometry. Lower normalized values generally corresponded to specimens that failed by jump-out, which were typically characterized by shorter thread engagement lengths and larger casing diameters. Higher normalized values were more commonly associated with rupture failures, which occurred in specimens with longer thread engagement lengths and smaller diameters, consistent with a greater degree of section plastification prior to failure.

The largest discrepancies between observed capacities and plastic moment predictions were observed for specimens with the largest casing diameter of 346 mm. For these specimens, the ratio M_u/M_P ranged from approximately 0.58 to 0.96, indicating that even plastic capacity-based predictions tend to overestimate flexural strength for large-diameter micropiles. This behavior reflects the increased susceptibility of larger diameters to jump-out failure, driven by reduced hoop strain requirements for a given level of box dilation. Consequently, while plastic moment capacity provides a more physically consistent basis for estimating flexural strength than the 50% rule, the results indicate that it should not be directly applied to larger-diameter micropiles without additional refinement that accounts for joint kinematics and failure mode.

An important trend identified in the test results is that joint strength, when normalized by the plastic moment capacity of the pin-end section, M_P, decreases as casing diameter increases. Larger-diameter micropiles were observed to be more susceptible to jump-out failure, a behavior that can be explained directly through joint kinematics. Jump-out occurs when radial displacement of the box-end reaches the thread face contact height, such that $u_r = h$. The corresponding hoop strain required to achieve this dilation is given by $\varepsilon_\theta = \frac{2u_r}{D} = \frac{2h}{D}$. Because the thread height, h, was held constant for all casing diameters in the experimental program, larger-diameter casings required smaller hoop strains to reach the critical dilation necessary for jump-out.

This effect is illustrated by comparing the strain levels required for different diameters. For casings with $D = 194$ mm, jump-out corresponds to a hoop strain of $\varepsilon_\theta = 2 \times 2.3/194 = 0.0237$, whereas casings with $D = 244$ mm require only $\varepsilon_\theta = 2 \times 2.3/244 = 0.0189$. As a result, larger-diameter micropiles reach jump-out failure at lower strain levels than smaller-diameter specimens, even when thread geometry and engagement length are similar. This fundamental geometric effect explains the increasing discrepancy between observed capacities and plastic moment predictions for larger diameters.

Based on these observations, lower-bound estimates for joint flexural capacity can be proposed to account for the increased likelihood of jump-out for larger casings using thread heights investigated in this study. For micropiles with casing diameters $D \leq 244$mm, a conservative lower-bound capacity may be taken as $M_u = M_P$. For larger diameters, where jump-out becomes more prevalent, even for larger thread lengths, a reduced capacity of $M_u = 0.8M_P$ is

recommended. Higher capacities may be justified when rupture is known to govern, which was observed for all specimens with $D \leq 244$mm and relative thread engagement lengths $L/D \geq 0.2$, as well as for type C threads regardless of engagement length due to their resistance to thread slip.

In cases where failure occurred at the box-end—specifically for type B threads with a casing diameter of 178 mm, where the box wall thickness was smaller than that of the pin-end—the flexural capacity is better represented by the plastic moment capacity of the box section, $M_{P,\mathrm{box}}$. Adoption of these revised capacity estimates resulted in a mean squared residual error (MSRE) of 62 kNm, representing an approximate 25 % improvement relative to the MSRE of 81 kNm obtained using the conventional 50 % wall-thickness rule.

These results demonstrate that more accurate estimation of micropile joint strength requires explicit consideration of joint kinematics, including box dilation, hoop strain development, and thread slip mechanisms. While the proposed bounds offer a practical improvement over existing design approaches, the findings also underscore the need for the development of physically consistent predictive models that directly incorporate thread geometry and deformation mechanisms to reliably predict both failure mode and flexural strength of threaded micropile connections. Ultimately this comes down to the specific thread design associated with a particular micropile size/diameter. While results presented in this study cannot be generalized to all piles, the failure modes and associated kinematics that should be considered have been elucidated via the detailed measurements obtained near joints in this study.

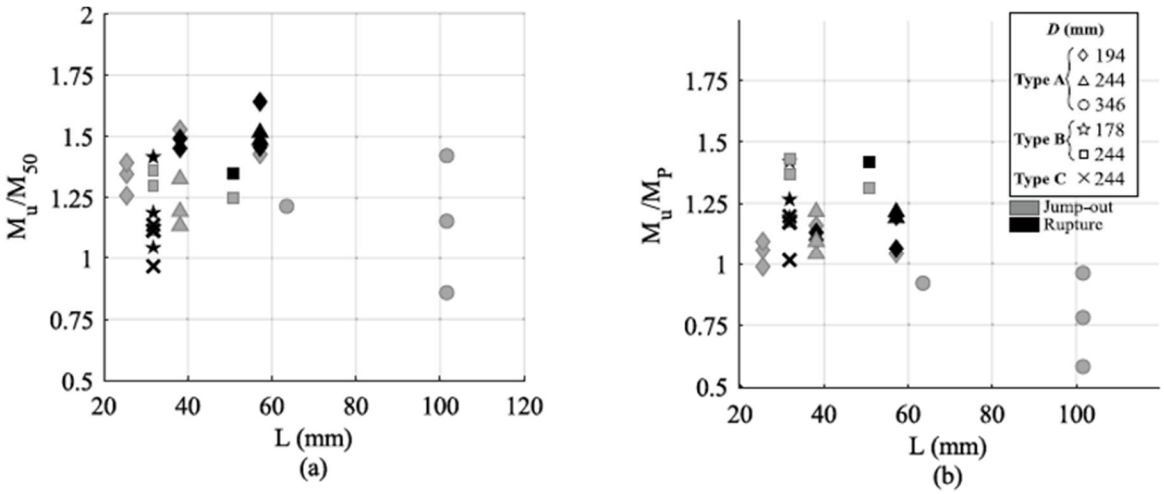

Figure 14. Observed to predicted strength ratio based on: (a) 50 %-Rule (M_{50}); and (b) plastic section capacity of the pin-end (M_P). (from Montoya-Vargas et al. 2025a)

2.3: Summary and Discussion

Section 2 presented a comprehensive experimental investigation into the flexural capacity and failure mechanisms of micropile threaded connections subjected to pure bending. A total of 31 grout-filled steel micropiles were tested under controlled four-point bending conditions to isolate joint behavior and eliminate confounding effects from shear or localized boundary conditions. The experimental configuration was intentionally selected to induce near-pure bending at the threaded

connection, enabling direct observation of joint-level kinematics and failure processes. A broad range of casing diameters, thread geometries, wall thicknesses, and thread engagement lengths were examined to capture the influence of connection details commonly encountered in practice.

Flexural behavior is governed by localized deformation mechanisms at the joint, including thread slip, box-end dilation, hoop strain development, and axial strain accumulation. These mechanisms were shown to control both stiffness degradation and ultimate failure mode. Two distinct failure modes were consistently observed:

1. Jump-out, characterized by thread slip and joint decoupling driven by box dilation.
2. Rupture, characterized by axial strain localization and tensile cracking while thread engagement was maintained.

Importantly, global moment–deflection response alone was insufficient to distinguish between these failure modes, underscoring the necessity of local measurements. High-resolution three-dimensional Digital Image Correlation (DIC) proved critical for identifying the governing kinematics. Full-field displacement and strain measurements revealed that box-end dilation and associated hoop strains dominate jump-out failures, whereas rupture failures are controlled primarily by axial strain development and section plastification. Thread geometry and wall thickness were found to directly influence these responses: shorter thread engagement lengths, thinner box walls, and inclined thread faces promoted dilation and jump-out, while longer engagement lengths and square-thread geometries inhibited slip and favored rupture. These observations were consistent across thread types and casing sizes, though the magnitude and spatial distribution of strains varied.

Results from pure bending tests also highlighted systematic shortcomings in the widely used 50% wall-thickness rule for estimating flexural capacity. Experimental capacities exhibited substantial variability relative to predictions based on this assumption, with consistent underestimation of strength and no ability to predict governing failure modes. The data clearly demonstrate that joint strength cannot be reliably inferred from nominal section properties alone. Instead, it depends on the interaction between geometry, material response, and joint-level kinematics, particularly box dilation and hoop strain demand. These are intimately linked to the specific thread geometry and material properties.

Regardless, this portion of the study establishes a mechanistic foundation for understanding the flexural behavior of micropile threaded connections under pure bending. The results show that failure is governed by deformation compatibility and joint kinematics rather than simple sectional yielding, and that connection geometry plays a decisive role in both strength and failure mode. Moreover, lessons learned from these tests can be carried over to better predict performance under common loading conditions for foundations like combined bending and compression—which is the subject of the next section.

Chapter 3: Flexural Capacity Under Combined Loading

Results from pure bending tests demonstrated that flexural capacity at threaded micropile joints is governed by tensile-driven failure mechanisms rather than by uniform section yielding (Zanuy et al., 2012; Montoya-Vargas et al., 2025a). In practice, however, micropiles are rarely subjected to bending alone. Many applications—including offshore structures, transmission towers, wind turbine foundations, and integral abutment bridges—impose combined axial compression and bending demands (Sabatini et al., 2005; Matos et al., 2016; Cerfontaine et al., 2023). Conventional structural design approaches, such as those codified by AASHTO and AISC, address combined loading using axial–flexural interaction equations developed for continuous steel members and therefore predict reduced flexural capacity with increasing axial compression (AASHTO, 2017; AISC, 2022). When applied to threaded micropile joints, these approaches would predict even further reductions in flexural capacity relative to pure bending.

While this assumption is generally valid for uniform micropile sections, its applicability to threaded connections is questionable. Unlike continuous sections, threaded joints fail through tensile-controlled kinematics, where box dilation, joint seam opening, and thread disengagement govern strength (Zanuy et al., 2012; Montoya-Vargas et al., 2025a). Experimental observations from pure bending tests indicate that compressive axial stresses are expected to delay tensile strain development and suppress the kinematic processes leading to jump-out or rupture, rather than accelerate them (Montoya-Vargas et al., 2025a). As a result, axial compression may increase—rather than decrease—the flexural capacity of threaded connections, contrary to standard design expectations based on continuous-member behavior.

Building on the mechanistic observations established from pure bending tests presented in Section 2 of this report, this section examines the influence of axial compression on the flexural behavior and capacity of threaded micropile joints under combined loading. To this end, augmented four-point bending tests were conducted using the same rigorous experimental techniques employed in the pure bending study, including full-scale testing and three-dimensional Digital Image Correlation, to directly quantify joint behavior under combined flexure and compression.

3.1 Materials and Methods

This study considers a total of 19 grout-filled steel micropile specimens incorporating a single threaded joint. Of these, 10 specimens were previously tested under pure bending conditions (Previous section and Montoya-Vargas et al. 2025a). The remaining nine specimens were subjected to combined axial compression and bending, achieved by first applying a compressive axial load and subsequently loading the specimens in a four-point bending configuration, as illustrated in Figure 15. This combined loading protocol was selected to evaluate the influence of axial compression on flexural behavior, joint kinematics, and ultimate capacity of threaded micropile connections.

The experimental procedures and instrumentation for the combined loading tests closely followed those established for the pure bending program (Montoya-Vargas et al., 2024; Montoya-Vargas et al., 2025a), including specimen geometry, support conditions, loading configuration, and measurement techniques. The primary distinction in the present test series was the introduction of

axial preloading prior to application of bending moments. A detailed description of the testing procedures, instrumentation layout, boundary conditions, and specimen fabrication is provided by Montoya-Vargas et al. (2025b). In this section, only a brief overview of the experimental setup is presented, with emphasis placed on features and procedures unique to the combined axial–flexural loading scenario.

All tested specimens consisted of two 1.5 m long steel casing segments connected by a single threaded joint located at mid-span. Specimen assembly was intended to replicate typical field construction procedures for micropiles, including application of make-up torque, T, using a hydraulic wrench to fully engage the threaded connection (Sabatini et al., 2005; Montoya-Vargas et al., 2024, 2025a). Following assembly and torquing, the casings were positioned vertically and gravity grouted.

The grout consisted of a cementitious mix with a water–cement ratio of 0.3. Mean grout compressive strength, f_c', was determined by testing 50 mm cube specimens cast from each grout batch in accordance with standard practice, with measured strengths summarized in Table 3 (Montoya-Vargas et al., 2025b). This grouting procedure was consistent across both pure bending and combined loading specimens to ensure comparability of joint behavior.

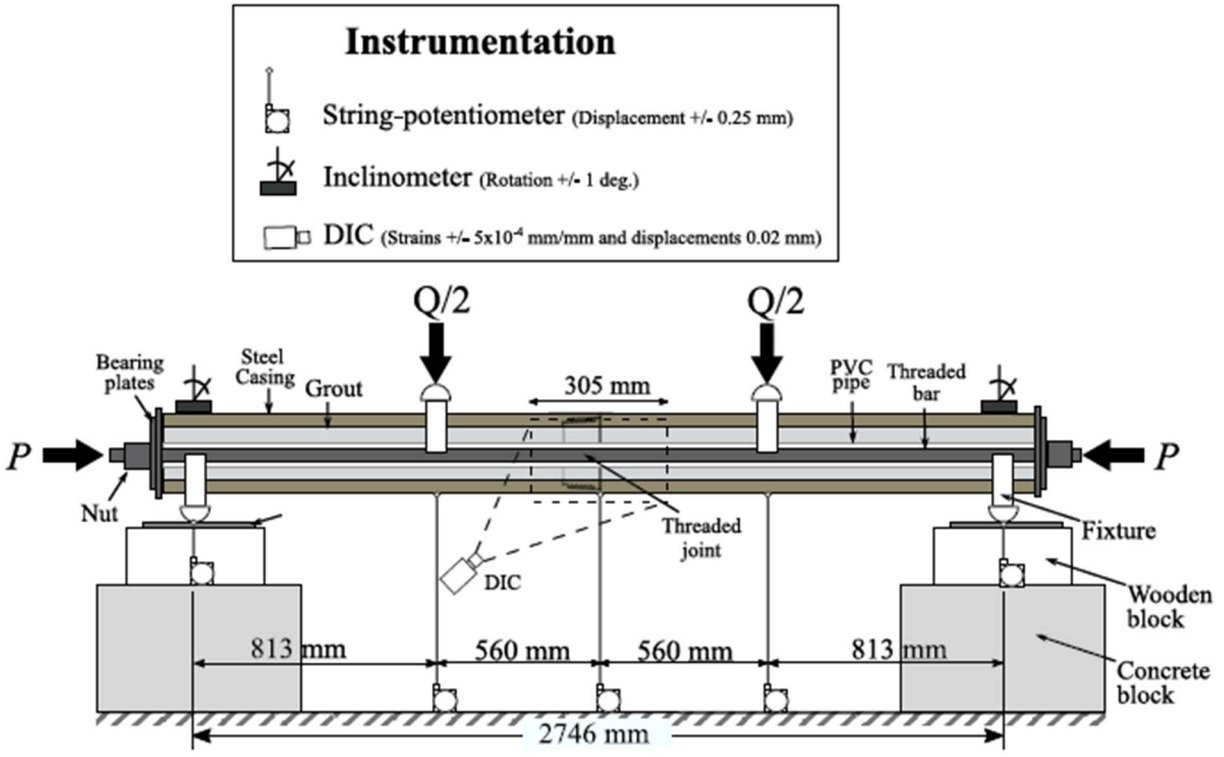

Figure 15. Test configuration, components, dimensions, and instrumentation used during four-point bending tests of micropiles, where axial compression was applied prior to bending.

Table 3. Casing specimen geometries and material strength properties.

D (mm)	t (mm)	L (mm)	h (mm)	$\tan\gamma$	t_1 (mm)	t_2 (mm)	f_y (MPa)	f_u (MPa)	f'_c (MPa)	Test IDs
244	13.8	38.1	2.4	0.0625	7.1	5.8	932	989	55	1 to 6
244	13.8	57.2	2.4	0.0625	7.5	6.6	932	989	55	7 to 10
244	13.8	31.2	2.6	0	5.1	5.1	700	802	69	11 to 15
244	13.8	50.8	2.6	0	5.1	5.1	700	802	69	16 to 19

For specimens tested under combined loading, a 50.8 mm (2-in.) diameter PVC pipe was installed concentrically within the casing prior to grouting. The region inside the PVC pipe was intentionally left ungrouted and served as a conduit for a post-tensioning bar used to apply compressive axial load to the specimen during testing (Figure 15). This configuration allowed axial compression to be introduced independently of bending while maintaining identical external geometry, boundary conditions, and joint details relative to the pure bending specimens (Montoya-Vargas et al., 2025b).

Axial compressive loads were applied to the micropile specimens using a post-tensioning procedure prior to the application of bending. The post-tensioning system consisted of an unbonded, cold-rolled, high-strength steel threaded bar installed concentrically within the PVC conduit described previously and secured to the micropile using bearing plates and mechanical fasteners at each end of the casing (Figure 15). The configuration and individual components of the post-tensioning system, including the threaded bar, bearing plates, anchorage hardware, and reaction elements, are illustrated schematically in Figure 16. Axial load was introduced by tensioning the bar using a hydraulic jack acting against a reaction plate, after which the anchorage hardware was tightened firmly against the bearing plate at the end of the micropile so that the tensile force in the bar was transferred to the micropile as a compressive axial load once the jack was removed.

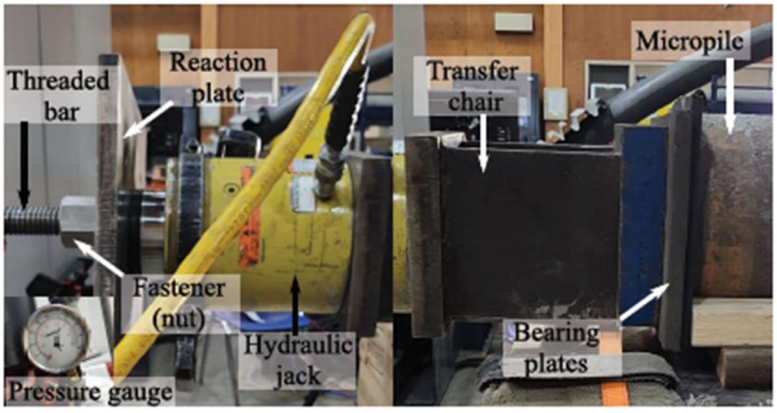

Figure 16. Components of the post-tensioning system used to apply axial load to micropile casings.

The post-tensioning bar had a nominal diameter of 45 mm and a tensile capacity of 845 kN. Target axial loads, P, ranging from 540 to 670 kN—corresponding to approximately 62 to 80 % of the bar's tensile capacity—were selected to ensure the bar remained elastic throughout testing and that the applied axial force could be maintained during subsequent four-point bending. Applied axial loads were monitored indirectly through measurement of hydraulic fluid pressure in the jack and converted to axial force using the jack calibration curve. The axial loads applied to each specimen were maintained during bending and are summarized later alongside the experimental results.

During four-point bending, lateral load, Q, was applied under displacement control at a constant rate of 6 mm/min until failure of the threaded joint occurred. Global specimen response was monitored using string potentiometers and inclinometers to measure deflections and rotations near mid-span and at the specimen ends, consistent with the instrumentation employed in the pure bending program. In addition, localized displacement and strain fields in the vicinity of the threaded joint were measured using three-dimensional Digital Image Correlation (DIC), enabling detailed assessment of joint-level kinematics during loading (Figure 15). This instrumentation strategy allowed simultaneous evaluation of global flexural response and localized deformation mechanisms under combined axial–flexural loading.

All specimens were fabricated from Grade 80 steel casing with a nominal yield stress of 550 MPa. Actual yield strength, f_y, and ultimate tensile strength, f_u, were provided by the manufacturer and verified through coupon tension tests conducted in accordance with ASTM A370. At present, no standardized design methodology exists for micropile thread geometry; therefore, the threaded connections evaluated in this study were based on prevailing industry practice. All casings had an outer diameter of $D = 244$ mm and an unthreaded wall thickness of $t = 13.8$ mm, with threaded regions incorporating variations in wall taper angle (γ), pin-end wall thickness (t_1), box-end wall thickness (t_2), and thread engagement length (L). Threaded joints with both tapered-wall (TW) and non-tapered-wall (NTW) configurations were included as part of a broader experimental program aimed at evaluating the influence of thread geometry on flexural capacity, though these variations were not the primary focus of the combined loading study. The previous section of the report demonstrated the sensitivity of flexural response under pure bending to thread length, wall taper, wall thickness, and thread shape; the same thread geometries were therefore adopted in the combined loading portion of the study to enable direct comparison between pure bending and combined loading conditions. The thread geometries are illustrated in Figure 17 and summarized in Table 3, along with the corresponding steel material properties (f_y and f_u) and grout compressive strength (f_c') for each tested specimen.

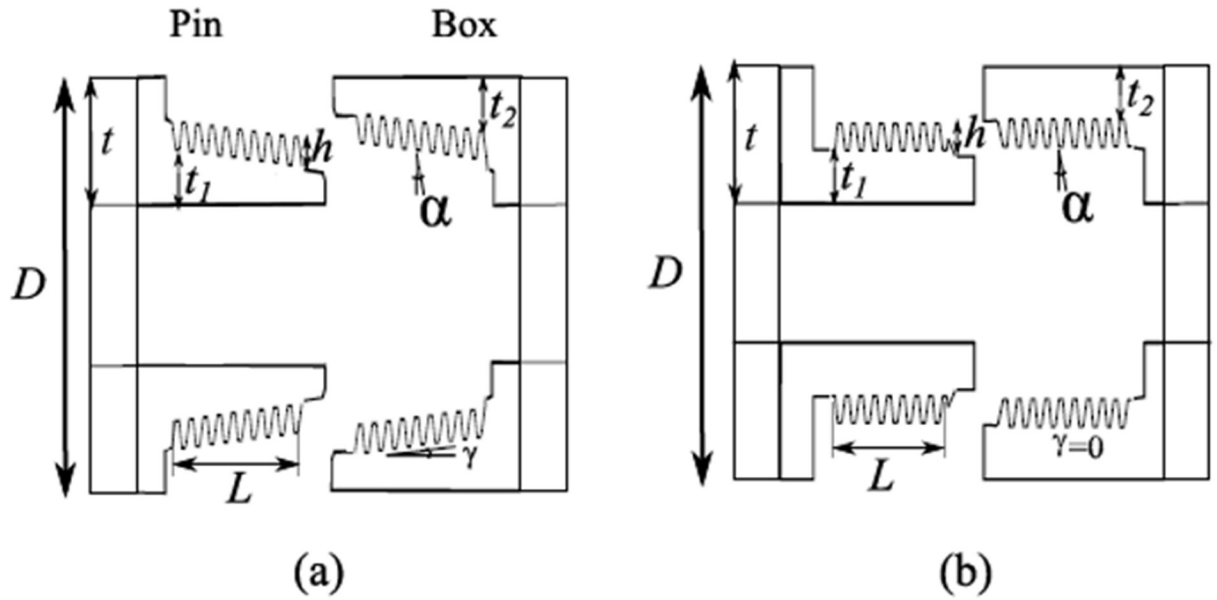

Figure 17. Threaded joint geometries indicating micropile diameter (D), nominal wall thickness (t), thread wall thicknesses (t1 and t2), thread length (L), thread wall taper angle (γ), and thread face inclination (α = 30 ◦) for: a.) tapered thread wall (TW) joint and b.) non-tapered thread wall (NTW) joint.

3.2 Test Results for Combined Loading

Load-Deflection Behavior

The relationship between mid-span deflection, z_B, and applied mid-span bending moment, M, is shown in Figure 18a for two representative specimens with differing thread engagement lengths tested under combined axial compression and bending. For comparison, corresponding moment–deflection responses reported by Montoya-Vargas et al. (2025a) for specimens with identical thread details tested under pure bending are also included. In addition, theoretical moment–deflection responses for a continuous micropile without a mid-span joint are shown as reference cases. These include solutions accounting for first-order geometric effects under pure bending and second-order geometric nonlinear effects when axial compression is present, providing a baseline for interpreting stiffness degradation and joint-controlled behavior observed in the experiments.
The theoretical mid-span deflection considering only first-order effects is given by the classical closed-form solution for a four-point bending configuration (Timoshenko & Gere, 1961),

$$z_B = \frac{Qa}{48EI}(3H^2 - 4a^2) \tag{6}$$

where Q is the applied lateral load at each load point, $a$is the distance from the applied load to the nearest support, H is the total span length, E is the elastic modulus of the steel casing ($E = 200$ GPa), and I is the moment of inertia of the casing assuming a continuous section with no joint ($I = 6.69 \times 10^{-4}$ m^4). When axial compression is present, second-order geometric effects are accounted for using

$$z_B = \frac{Qa}{2EI\lambda^2}\left[\frac{2\sin(\lambda a)\sin\left(\frac{H}{2}\right)}{\lambda a \sin(\lambda H)} - 1\right] \quad (7)$$

where $\lambda = \sqrt{P/EI}$ is the stability parameter associated with axial load. Under combined loading, the bending moment at the threaded joint is influenced not only by the applied lateral load but also by the axial compression acting through the lateral deflection at mid-span. Accordingly, the applied moment at the joint is given by,

$$M = \frac{Qa}{2} + Pz_B \quad (8)$$

where P is the applied axial compressive load and z_B is the corresponding mid-span deflection.

These theoretical responses provide a useful reference for evaluating deviations in stiffness and deflection behavior attributable to the presence of the threaded joint and the interaction between axial compression and joint-level kinematics. Moment–deflection responses exhibited a linear relationship at low load levels and were well approximated by first-order elastic theory for bending moments up to approximately 20–35 kNm for specimens subjected to pure bending (Figure 18b). In contrast, specimens tested under combined axial compression and bending exhibited noticeably higher initial stiffness in the M–z_B response due to second-order effects. This increased stiffness is attributed to the presence of axial compression delaying the onsite of joint kinematics associated with tensile mechanisms (previous section).

Improved agreement between measured and theoretical deflections for axially loaded specimens was obtained by modifying the second-order analytical solution to account for a transformed section moment of inertia of $I = 8.13 \times 10^4 cm^4$, which reflects the increased stiffness contribution of the grout under compression. Using this adjusted inertia, theoretical predictions closely matched experimental responses for bending moments below approximately 75 kNm (Figure 18b). Beyond this level, nonlinear behavior became evident, characterized by a reduction in stiffness and a change in slope of the M–z_B curve (see M_s on Figure 18b), followed by abrupt failure of the threaded joint at much larger loads (Figure 18a). In all cases, failure was localized at the threaded connection, with no evidence of yielding or damage occurring away from the joint region.

Figure 18c illustrates the generalized moment–deflection response observed across the test program using a piecewise representation. At low bending moments, the response initially follows the predicted behavior of a continuous, jointless casing, with system stiffness governed by the intact section properties. This behavior persists for bending moments below a threshold value denoted as M_s. Once the applied moment exceeds M_s, the threaded connection transitions from behaving as a rigid joint to a semi-rigid connection. This transition is accompanied by a reduction in stiffness, reflected by a decrease in the slope of the moment–deflection curve, and a nonlinear response that continues until ultimate failure occurs at a moment M_f.

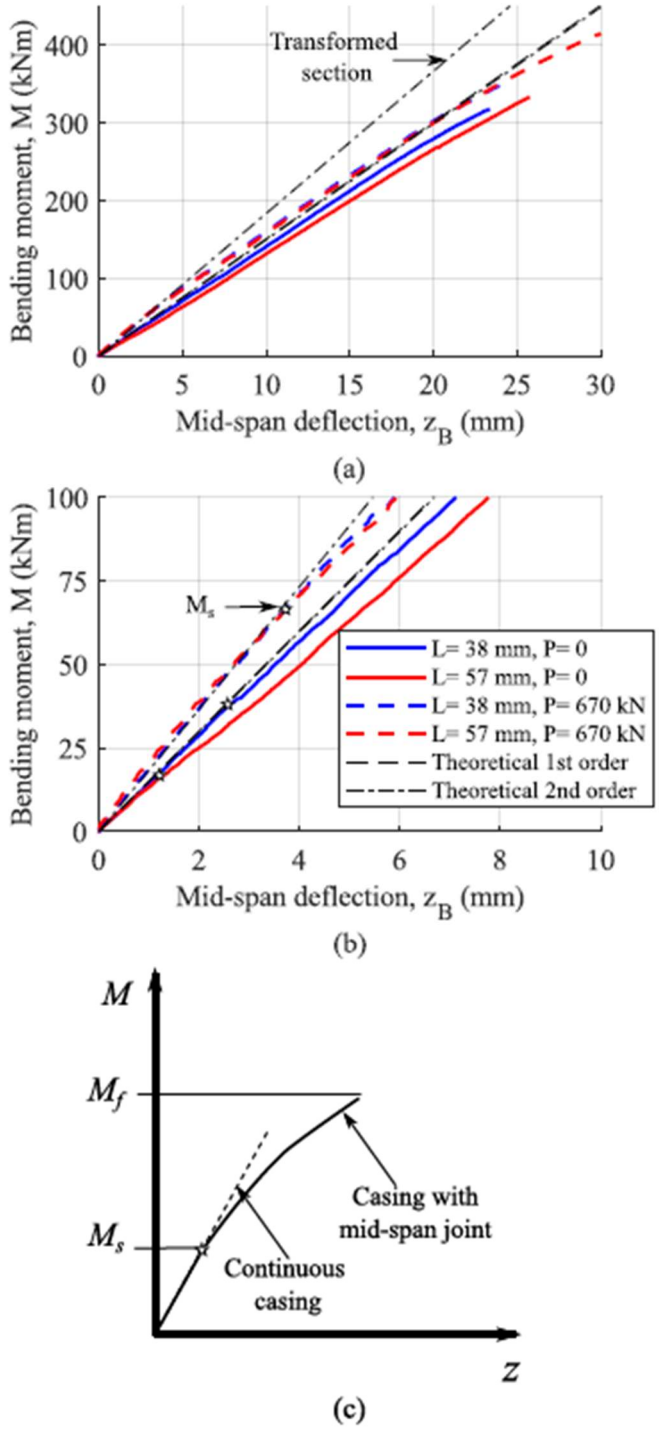

Figure 18. a.) Mid-span bending moment, M, vs. vertical deflection, zB, for tapered wall joints with different thread lengths and loading conditions (i.e. with and without axial load). b.) Same as above but illustrating the moment (Ms) where there is a slope change in the M − ZB curve and deviation from theoretical predictions for a continuous section of casing. c.) Conceptual illustration of Ms and Mf . The data in (a) and (b) above are for TW specimens with Test IDs 1, 5, 7, and 10.

Representative examples of this stiffness transition are shown in Figure 18a and Figure 18b. Under pure bending, specimens 5 and 10 (solid lines) exhibited a reduction in stiffness from approximately 15.4 kNm/mm to 12.5 kNm/mm as the joint response softened. Similarly, under combined axial compression and bending, specimens 4 and 7 (dashed lines) transitioned from initial stiffness values of approximately 18.7 kNm/mm to about 13 kNm/mm. This piecewise response was consistent across all specimens regardless of the presence or magnitude of axial compression. Differences among specimens were primarily reflected in the magnitudes of the threshold moment M_s and the failure moment M_f, both of which were strongly influenced by the applied axial compressive load, P, and to a lesser extent by the make-up torque, T, applied during joint assembly. Although the post-tensioning bar experienced bending due to rotation at the micropile ends, its contribution to overall system stiffness and strength was negligible owing to its relatively small diameter compared to the steel casing.

The threshold moment $M_s$was systematically identified by evaluating changes in stiffness along the measured moment–deflection (M–z_B) response. This was accomplished by fitting a linear (first-degree) polynomial to a moving window of data points along the M–z_B curve and computing the tangent stiffness at the midpoint of each window. In this manner, the transition from the initial linear response to the reduced-stiffness regime could be more clearly identified, with $M_s$defined as the moment at which the tangent slope stabilized following its initial reduction. A sensitivity analysis was performed to assess the influence of window size on the calculated slope, and a window of 100 data points—corresponding to approximately 10 kNm—was found to effectively capture the stiffness transition while minimizing noise-related variability. Figure 19a presents a comparison of the resulting $M_s$values for specimens tested under pure bending and those subjected to combined axial compression and bending.

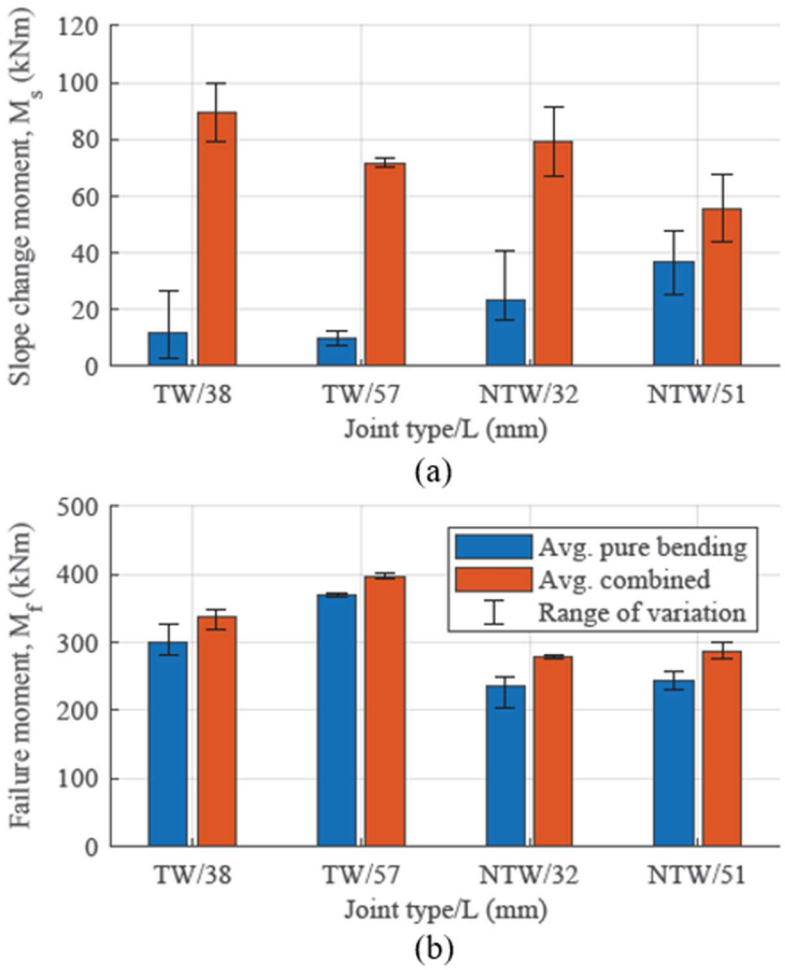

Figure 19. Comparison of bending moments under pure bending and combined loading at different loading stages: a.) slope change in $M-zB$ curve (Ms); and b.) at failure (Mf).

As shown in Figure 19a, the threshold moment M_s was consistently higher for specimens tested with applied axial compression, indicating that the micropiles behaved as effectively "continuous" members over a larger range of transverse loading. This trend is consistent with the tensile-controlled failure mechanisms identified for threaded joints under pure bending (Montoya-Vargas et al., 2025a). Because compressive axial stresses must be overcome before tensile stresses can develop at the joint, the onset of tensile thread engagement—and the associated joint kinematics leading to stiffness degradation—was delayed. This delay in tensile engagement not only shifted the stiffness transition to higher bending moments but also resulted in a systematic increase in ultimate flexural capacity, M_f, for specimens tested under combined loading relative to those tested in pure bending, as illustrated in Figure 19b.

Table 4 summarizes the threshold moment M_s and ultimate flexural capacity M_f for all tested specimens, along with the corresponding applied axial compressive load, P, and make-up torque, T, used during specimen assembly. These data provide a comprehensive basis for evaluating the relative influence of axial compression and joint assembly conditions on stiffness transition and failure behavior under combined loading.

Table 4. Summary of the makeup torque (T), axial load (P), slope change moment (Ms) and failure moment (Mf) for each four-point bending test performed.

Test ID	Joint type/ L -/(mm)	T (kNm)	P (kN)	M_s (kNm)	M_f (kNm)
1	TW/38.1	12.6	670	88.9	348
2		13.5	541	78.9	319
3		14.3	541	99.7	345
4	TW/38.1	10.4	0	6.0	280
5		12.1	0	2.6	327
6		13.8	0	26.5	294
7	TW/57.2	11.8	670	70.1	401
8		10.3	630	73.3	393
9	TW/57.2	10.0	0	12.5	373
10		11.0	0	7.1	366
11	NTW/31.2	16.2	541	66.8	276
12		12.9	541	91.2	282
13	NTW/31.2	14.9	0	40.6	248
14		15.3	0	16.1	239
15		12.8	0	16.7	250
16	NTW/50.8	15.1	670	43.7	275
17		16.4	541	67.4	299
18	NTW/50.8	11.4	0	25.4	230
19		11.8	0	47.6	258

DIC Measurements

Digital Image Correlation (DIC) measurements provided detailed insight into joint kinematics and load transfer mechanisms across the threaded connection throughout the loading process. Figure 20 presents representative axial strain fields, ε_x, for specimens tested under pure bending (left column) and combined axial compression and bending (right column). Strain fields are shown at bending moments of $M = 30, 50, 300$, and 327 kNm to illustrate the evolution of strain distribution within the threaded region under both loading conditions. For specimens tested under combined loading, bending-induced strains are superimposed on a uniform axial compressive strain, ε_0, resulting from the applied pre-compression (right column of Figure 20). For specimen 1, tested with an applied axial load of $P = 670$kN, the compressive strain associated with preloading was estimated as $\varepsilon_0 = P/(EA) = 250$, where $A = 615$ mm^2 represents the transformed section area accounting for the combined stiffness contributions of the steel casing and grout.

At a bending moment of $M = 30$ kNm (Figure 20a), both specimens exhibited tensile axial strains that were relatively uniformly distributed along the threaded region, with limited localization and

only minor fluctuations attributable to measurement noise (approximately ±100 $\mu\varepsilon$). At $M = 50$ kNm, differences in strain distribution became evident between loading conditions. For the specimen subjected to pure bending (Figure 20b, left), tensile strains became less evenly distributed and began to localize in threads located farther from the joint seam ($x \approx -30$ mm). This redistribution coincided with exceedance of the stiffness transition threshold, $M_s = 34.8$ kNm and reflects the onset of joint separation on the tension side, where reduced load transfer occurred near the joint seam and increased load transfer developed in threads farther away. In contrast, the specimen tested under combined axial compression and bending exhibited more uniform tensile strain distributions at both $M = 30$ and 50 kNm (Figure 20a and Figure 20b, right), with overall lower tensile strain magnitudes due to the presence of pre-compression. For this specimen, the applied bending moment remained below the corresponding stiffness transition threshold ($M_s = 79.6$ kNm), and tensile stresses continued to be transferred more uniformly across the threaded connection.

For bending moments well in excess of the stiffness transition threshold, M_s, both specimens exhibited similar axial strain distributions, as shown in Figure 20c. This convergence in strain behavior indicates that once the compressive pre-stress is overcome and separation initiates at the joint seam on the tension side, the governing load-transfer mechanisms and joint kinematics under combined axial–flexural loading become comparable to those observed under pure bending. In this regime, both specimens exhibited substantially reduced tensile strains in the immediate vicinity of the joint seam, accompanied by pronounced compressive strain concentrations near the seam. Conversely, the largest tensile strains developed farther away from the seam toward the opposite end of the threaded region, while the spatial extent of the compressive strain concentration near the seam decreased.

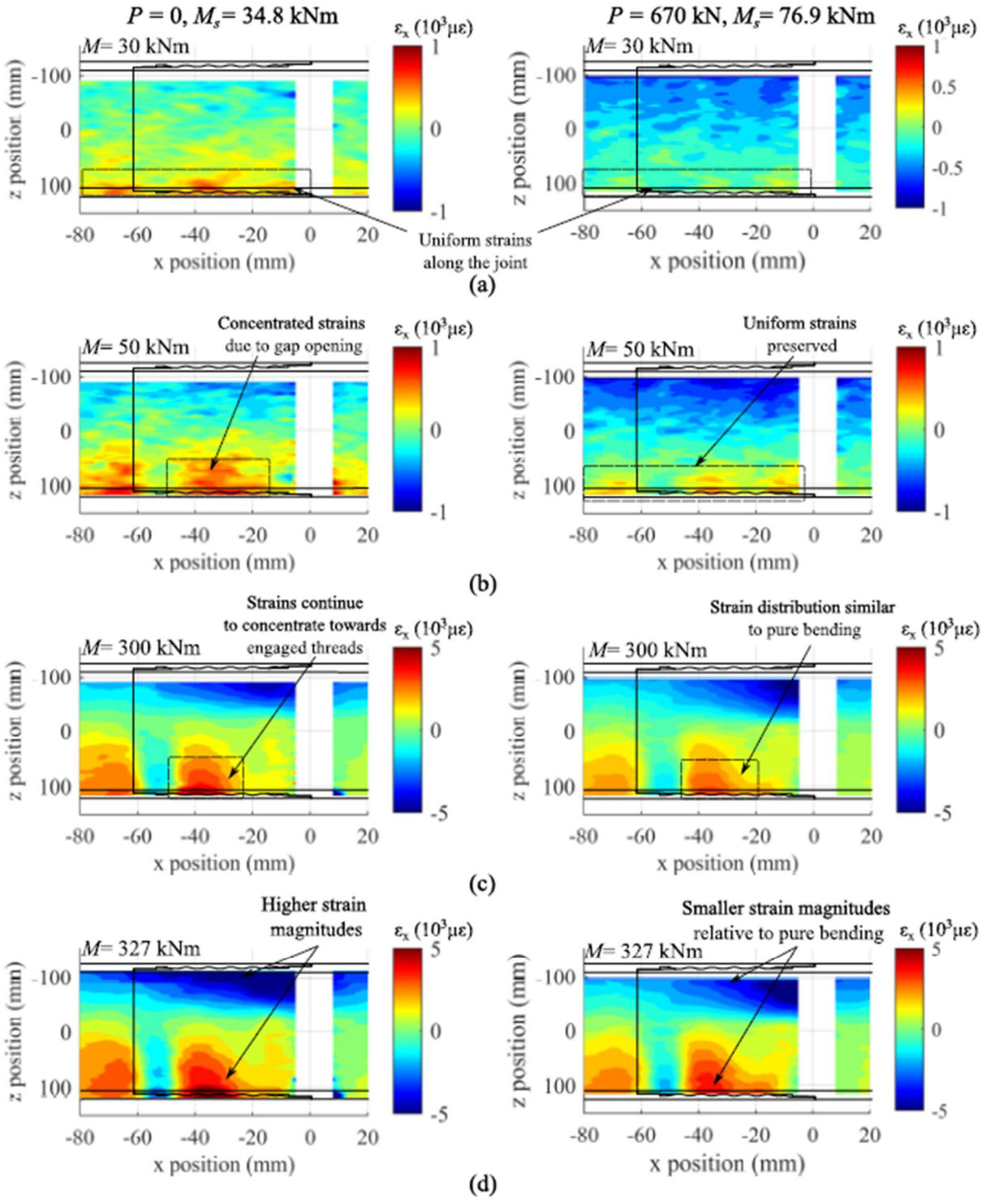

Figure 20. Comparison of axial strain fields (εx) from DIC measurements at threaded connections for pure bending (specimen 1, left) and combined axial and bending (specimen 5, right) at different load levels: a.) M = 30 kNm; b.) 50 kNm; c.) 300 kNm; and d.) 327 kNm (failure load for pure bending). Thread details for each specimen are identical.

These trends became more pronounced at higher load levels, as illustrated by the strain fields at $M = 327$ kNm in Figure 20d. At this load level, the specimen tested under pure bending failed in tension and exhibited higher tensile strain magnitudes relative to the specimen tested under combined loading. The specimen subjected to combined axial compression and bending continued to sustain additional load and ultimately reached a higher flexural capacity of $M = 348$ kNm. Comparable strain evolution patterns were also observed for non-tapered wall (NTW) threaded joints, indicating that the general kinematic response under combined loading is consistent across thread geometries. Differences between tapered-wall (TW) and NTW joints were primarily associated with the magnitude and distribution of hoop strains, which are not discussed here for brevity. The influence of wall taper on joint kinematics and failure behavior is examined in greater detail elsewhere (Montoya-Vargas et al., 2025a).

Chapter 4: Prediction and Design

The experimental results presented in the preceding section demonstrate that flexural capacity under combined loading is governed by joint-level kinematics, particularly the interaction between axial compression, gap opening, and box-end dilation. Building on these observations, this chapter introduces an analytical framework for predicting flexural capacity of threaded micropile joints under combined axial compression and bending, grounded in the experimentally observed relationship between axial compressive loads and failure.

Key Considerations

To develop a tractable analytical model consistent with the experimentally observed joint behavior, the following assumptions were adopted:

- The micropile casing is idealized as a hollow circular section with outer diameter $D$and wall thickness t.
- The threaded joint is similarly idealized as a hollow cylinder with the same inner diameter, $D - 2t$, but with a reduced effective wall thickness t_1 reflecting the threaded region.
- The casing material is assumed to behave as elastic–perfectly plastic with yield stress f_y.
- Consistent with experimental observations, the ability of the joint to fully develop a plastic hinge is assumed to be governed by dilation of the box-end, which is controlled primarily by the ratio of box-end wall thickness to pin-end wall thickness, t_2/t_1.
- Finally, the ultimate flexural capacity of the joint, M_f, is assumed to scale directly with the moment required to initiate gap opening at the joint, M_s.

The rationale for these assumptions, and their integration into a predictive model, are described herein. As shown in Figure 21, experimental results indicate a clear relationship between flexural capacity and gap-opening moment, with M_f varying approximately linearly with M_s over the range of gap-opening moments observed in this study ($0 \leq M_s \leq 100$ kNm). On this basis, the flexural capacity of a threaded connection under combined loading is expressed as the sum of an inherent joint capacity and a component proportional to the gap-opening moment,

$$M_f = M_j + kM_s \tag{9}$$

where k is a proportionality parameter that modulates the influence of gap opening on ultimate capacity. For the limiting case in which $M_s = 0$, the joint capacity reduces to $M_f = M_j$, where M_j is defined as the flexural capacity of the threaded joint in the absence of axial pre-compression. This formulation provides a simple but physically motivated framework for incorporating the effects of axial compression, joint kinematics, and geometry into flexural strength predictions.

Thread interactions governing the inherent joint capacity, M_j, arise from the combined axial and hoop stress state that develops due to deformation compatibility between the pin- and box-ends of the threaded connection. These stresses are strongly influenced by thread geometry, wall thickness distribution, and engagement details, which control load transfer and strain localization within the joint (Montoya-Vargas et al., 2022; Montoya-Vargas et al., 2025a). Based on these considerations and supported by experimental observations, the inherent flexural capacity of the threaded joint is

assumed to be proportional to the plastic bending capacity of the pin-end section. Accordingly, $M_j$is expressed as,

$$M_j = \beta Z_p f_y \tag{10a}$$

where $Z_p$is the plastic section modulus of the pin-end, $f_y$is the steel yield stress, and $\beta$is a proportionality factor that accounts for the influence of thread details, casing size, and governing failure mode. Experimental results indicate that βvaries within the range $0.7 \leq \beta \leq 1.25$.
The plastic section modulus of the pin-end is computed as,

$$Z_p = \frac{(D-2t+2t_1)^3-(D-2t)^3}{6} \tag{10b}$$

where D is the outer diameter of the casing, t is the wall thickness of the unthreaded section, and t_1 is the effective wall thickness at the pin-end within the threaded region. For a given specimen, values of β appropriate for use in equation 10a may be estimated from experimental data as $\beta = \frac{M_j}{Z_p f_y}$, which requires prior determination of the inherent joint capacity, M_j. In practice, $M_j$should be evaluated only for joints assembled without applied make-up torque ($T \approx 0$) and tested under pure bending conditions ($P = 0$), as the presence of either torque or axial compression introduces pre-stress that results in nonzero gap-opening moments, M_s. This dependency of joint response on initial stress state has also been reported in experimental and numerical investigations of analogous threaded connections (Baragetti & Terranova, 2004).

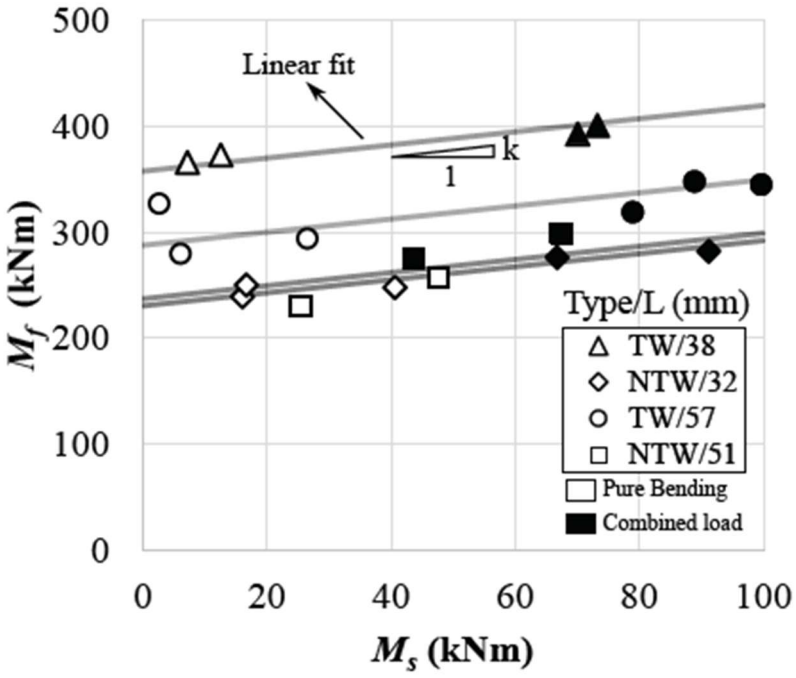

Figure 21. Observed joint bending capacity (Mf) as a function of the gap opening moment (Ms) for specimens with different thread details and loading conditions.

For specimens tested under pure bending conditions ($P = 0$), the gap-opening moment, M_s, may be conservatively assumed to be zero. However, experimental results indicate that specimens subjected to pre-compression arising from make-up torque applied during joint assembly can exhibit nonzero values of M_s, even in the absence of externally applied axial load, as shown by the pure bending results in Figure 21. Based on the experimental study reported by Montoya-Vargas et al. (2025a), a value of $\beta = 1.0$ was recommended for casings with outer diameters $D \leq 244$ mm, while a reduced value of $\beta = 0.8$ was suggested for larger diameters. It is noted, however, that the influence of pre-compression contributing to gap opening was not explicitly isolated in that study; consequently, the proposed β values inherently reflect additional flexural capacity associated with nonzero M_s induced by torque applied during casing assembly.

In the present study, make-up torque representative of conventional construction practice was applied to all specimens. Accordingly, the inherent joint capacity, M_j, was estimated from the intercepts of the linear relationships between flexural capacity and gap-opening moment shown in Figure 21. The corresponding linear fit parameters and resulting estimates of β are summarized in Table 5. For these calculations, the plastic section capacity term $Z_p f_y$ was evaluated using the geometric and material properties reported in Table 3. This approach provides a consistent means of quantifying M_j while accounting implicitly for the effects of assembly-induced pre-compression present in practical micropile installations.

Table 5. Linear fit parameters Mj and k for the data shown in Figure 7 and corresponding parameter β estimated using equation 10a.

Type	L (mm)	k	M_j (kNm)	$Z_p f_y$ (kNm)	$\beta = \frac{M_j}{Z_p f_y}$	$\frac{t_2}{t_1}$
TW	38	0.62	288	330	0.87	0.82
TW	57	0.62	358	350	1.02	0.88
NTW	32	0.62	230	175	1.32	1
NTW	51	0.62	237	175	1.35	1

The semi-empirical parameter β is introduced to account for thread geometry and the complex kinematics and load transfer mechanisms at threaded connections that are not fully captured by the plastic section modulus, Z_p. These mechanisms include the extent of the box-end region subjected to compression and the degree of box dilation occurring on the tension side of the joint, both of which are strongly influenced by thread wall thickness, thread engagement length, and thread shape (discussed in Chapter 2 and Montoya-Vargas et al., 2025a). As summarized in Table 5, experimental results indicate that β scales with the ratio of box-end to pin-end wall thickness, t_2/t_1.

This relationship is well approximated by the empirical expression,

$$\beta = c\left(\frac{t_2}{t_1}\right)^d \tag{11}$$

where regression analysis of the experimental data yielded best-fit parameters of $c = 1.3$ and $d = 2.0$. Using these values resulted in an excellent fit to the measured data, with a coefficient of determination $R^2 = 0.99$ and a root-mean-square error (RMSE) of 0.03. Consistent with recommendations by Montoya-Vargas et al. (2025a), the parameter c may be reduced to account for increased susceptibility to jump-out in larger-diameter casings; casings with $D > 244$ mm.

Based on the experimentally observed relationship between the gap-opening moment, M_s, and the ultimate flexural capacity, M_f, shown in Figure 21, a proportionality factor of $k = 0.62$ was found to reasonably describe the influence of pre-compression arising from both applied axial load and make-up torque on joint strength. Accordingly, if the gap-opening moment can be measured or reliably estimated, equation 9 and 11 may be used together to predict the flexural capacity of threaded micropile joints under combined axial compression and bending.

The bending moment required to initiate gap opening at the threaded joint, M_s, is estimated by equating the tensile stress induced by bending to the compressive stresses generated by axial loading and make-up torque applied during casing assembly. Under this assumption, gap opening occurs when the combined compressive stress state is overcome, such that

$$M_s = (\sigma_T + \sigma_P)\, S_g \tag{12a}$$

where σ_T and σ_P are the axial compressive stresses induced by applied torque and axial load, respectively, and S_g is the elastic section modulus of the transformed steel–grout composite section. The section modulus is defined as,

$$S_g = \frac{\pi}{32D}\left[D^4 - \left(1 - \frac{1}{n}\right)(D - 2t)^4\right] \tag{12b}$$

In these expressions, it is assumed that both the steel casing and the infilled grout remain within the elastic range at the relatively low load levels associated with gap initiation. The modular ratio $n = E/E_c$ represents the ratio of the steel elastic modulus to the grout elastic modulus.

The compressive stress induced by the applied axial load is computed using transformed-section analysis as,

$$\sigma_P = \frac{P}{A_g} \tag{13a}$$

where the transformed cross-sectional area is given by,

$$A_g = \frac{\pi}{4}\left[D^2 - \left(1 - \frac{1}{n}\right)(D - 2t)^2\right] \quad (13b)$$

The axial pre-compression stress resulting from make-up torque, σ_T, is estimated using,

$$\sigma_T = \frac{1}{\mu\pi\ ^2(t_2 - L\text{ta}\ \ )}\left(T - \frac{\tau\pi\ ^2L}{2}\right) \quad (14)$$

where μ is the coefficient of friction at the shoulder contact surfaces, τ represents the frictional resistance mobilized along the thread faces, L is the thread engagement length, and γ is the wall taper angle. These interactions are assumed to be uniformly distributed around the thread perimeter. A detailed derivation and discussion of equation 14, including the assumptions underlying the torque-to-stress relationship, is presented by Montoya-Vargas (2025).

The friction parameters μ and τ appearing in equation 14 were estimated through inverse analysis by fitting the analytical predictions of gap-opening moment, M_s, to experimental results obtained from pure bending tests reported by Montoya-Vargas et al. (2025a). The calibration dataset included specimens with varying casing diameters and thread engagement lengths tested under pure bending conditions, providing a broad basis for parameter estimation. This approach allowed the combined influence of shoulder friction and thread-face friction on joint pre-compression to be inferred directly from measured changes slope of M-z_B curves.

It is noted that the best-fit values of μ and τ were obtained for specimens in which a thread compound (grease) was applied to tapered-wall threads to facilitate assembly, as provided by one supplier. In contrast, grease was not applied to non-tapered wall threads supplied by other manufacturers (Montoya-Vargas et al., 2025a). The resulting best-fit friction parameters are summarized in Table 6, which shows that lower values of the thread-face friction parameter τwere associated with greased threaded connections, as expected. In comparison, the estimated coefficients of friction at the shoulder interface, μ, were similar for both greased and non-greased joints and fall within the typical range reported for steel-on-steel contact (Grabon et al., 2018).

Table 6. Threaded joint frictional interaction parameters

Joint type	μ	τ (MPa)
Greased (Tapered Thread Wall)	0.23	0.12
Non-greased (Non-Tapered)	0.24	0.34

Gap-opening moments predicted using equation 12a are compared with experimentally observed values of M_s in Figure 22 for a range of joint configurations, casing diameters, and loading conditions. The comparison includes pure bending test results reported by Montoya-Vargas et al. (2025a), as well as the combined loading results from the present study. The predicted and measured gap-opening moments exhibit moderate agreement, with a correlation coefficient of $r = 0.62$and a root-mean-square error (RMSE) of 16 kNm. These results indicate that the proposed formulation captures some of the primary mechanisms governing gap initiation across different

joint types and loading scenarios, while also highlighting the inherent variability associated with joint assembly, precompression, and its influence on the slope change moment, M_s.

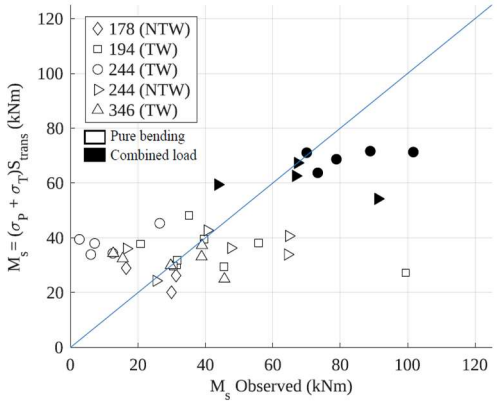

Figure 22. Predicted vs. observed Ms for different pile diameters and loading conditions.

Regardless, incorporating the effects of pre-compression through the gap-opening moment, M_s, improves the predictive performance of the proposed semi-empirical analytical model for flexural capacity of threaded micropile joints. Figure 23a compares predicted and observed joint failure moments, M_f, obtained using equations 9 through 14. The predictions exhibit strong agreement with experimental results, yielding a correlation coefficient of $r = 0.98$ and a root-mean-square error (RMSE) of 33 kNm. This comparison includes specimens with large casing diameters ($D = 346$ mm) reported by Montoya-Vargas et al. (2025a), for which the model adequately captures the mean flexural capacity despite the proportionally greater variability observed in the experimental data. Figure 23b further illustrates the predictive improvement through histograms of relative error, comparing predictions that include pre-compression effects via M_s with those that neglect pre-compression and assume $M_f = M_j$. When M_s is included, relative errors range from −0.25 to 0.30, with a near-zero mean error of 0.003. In contrast, neglecting M_s results in a wider error range (−0.35 to 0.25) and a larger average deviation of −0.09, indicating more conservative but less accurate predictions.

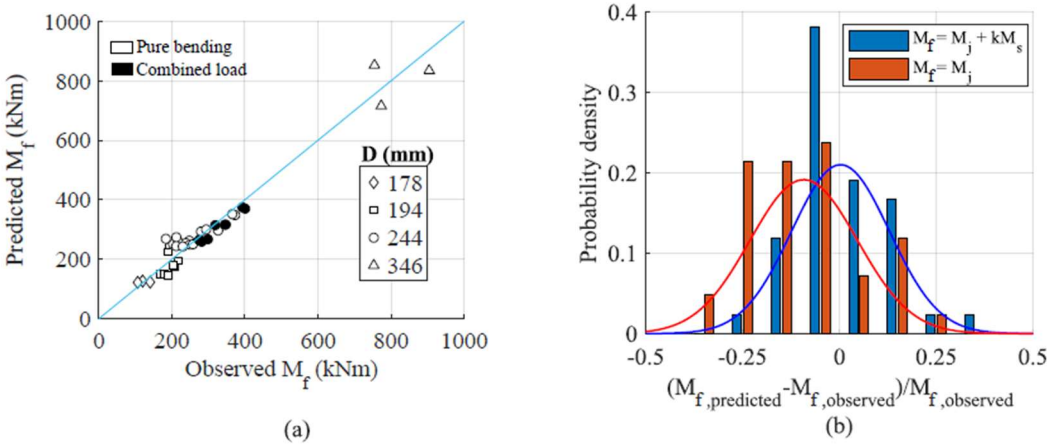

Figure 23. Predicted and observed joint bending capacities: a.) predicted vs. Observed Mf for different pile diameters and loading conditions when considering Ms; and b.) histogram of relative errors for predictions with and without the contribution of Ms.

Despite the improved performance associated with inclusion of M_s, notable discrepancies remain between predicted and observed gap-opening moments, particularly for specimens with $M_s < 25$kNm tested without externally applied axial load (Figure 22). The greatest source of uncertainty arises from quantifying the contribution of make-up torque applied during joint assembly. The calibrated friction parameters, μ and τ, implicitly assume uniform threaded joint conditions and uniform distribution of any applied thread compound; however, post-test inspection revealed that grease and contact conditions were often nonuniform, a condition that is likely in field installations also. Additional uncertainty is introduced by limitations in monitoring applied make-up torque using an analog dial gauge, where needle oscillations resulted in fluctuations of approximately ±10% from reported values. Further uncertainty may also arise from relaxation of torque-induced pre-compression during specimen handling, grouting, and placement in the test frame—effects that cannot be readily quantified. For specimens tested under combined loading, the application of axial compression likely reduced the relative contribution of torque-induced pre-compression to M_s, further complicating isolation of torque effects. Collectively, these factors highlight the inherent variability associated with joint assembly conditions and underscore the importance of explicitly accounting for pre-compression in predictive models while recognizing the limits of precision achievable in practice.

While make-up torque was incorporated in the preceding analyses to elucidate the influence of pre-compression on the gap-opening moment, M_s, and the resulting flexural behavior and capacity of threaded connections, its contribution is subject to considerable uncertainty. From a design perspective, it is therefore prudent to conservatively neglect the effect of torque on M_s and the onset of joint separation. In contrast, axial compressive loads can be quantified with a substantially higher degree of certainty. The experimental results presented herein demonstrate that axial compression does not necessarily reduce flexural capacity and can, in fact, increase the flexural strength of threaded micropile connections under combined loading.

Design Approach

Current design practice for micropiles subjected to combined axial load and bending requires that the factored bending moment, M_u, and factored axial load, P_u, satisfy a material interaction equation of the form prescribed by AASHTO and AISC (AASHTO, 2017; AISC, 2023),

$$c_1 \frac{P_u}{\phi_a P_n} + c_2 \frac{M_u}{\phi_b M_n} \leq 1 \tag{15}$$

where $P_n$and $M_n$are the nominal axial and flexural capacities of the micropile, respectively, and $\phi_a = 0.75$and $\phi_b = 1.0$are the corresponding strength reduction factors. The coefficients $c_1$and c_2 depend on the level of axial load: for $P_u/(\phi_a P_n) \leq 0.2$, $c_1 = 1/2$and $c_2 = 1$; for $P_u/(\phi_a P_n) \geq 0.2$, $c_1 = 1$ and $c_2 = 8/9$.

Although micropiles are typically grout filled, it is customary in design practice to evaluate axial and flexural capacity based solely on the steel casing. This assumption is supported by experimental evidence indicating that the grout provides negligible contribution to flexural capacity, as the steel casing reaches yield after the grout has already failed in compression

(Musselman et al., 2007; Froster et al., 2021). Accordingly, the nominal axial and flexural capacities are expressed as,

$$P_n = 0.85 f_y A_s \tag{16}$$

$$M_n = f_y S_j \tag{17a}$$

where f_y is the yield stress of the steel casing and $A_s = \pi[D^2 - (D - 2t)^2]/4$ is the cross-sectional area of the casing with outer diameter D and wall thickness t. The elastic section modulus at the threaded joint, S_j, is computed as,

$$S_j = \frac{\pi[(D-t)^4 - (D-2t)^4]}{32(D-t)} \tag{17b}$$

This formulation reflects the widely adopted "50%-Rule," in which the nominal wall thickness is reduced by 50% when computing bending capacity at threaded joints (Sabatini et al., 2005). Notably, the full wall thickness is retained in the axial capacity calculation, recognizing that threaded connections can transmit axial loads equivalent to the nominal casing thickness (Sabatini et al., 2005), whereas bending capacity is penalized to account for reduced tensile resistance at the joint. Although equation 17a represents a simplified characterization of joint behavior, it generally yields conservative estimates of flexural capacity under pure bending for common thread geometries (Montoya-Vargas et al., 2025a).

It follows directly from equation 15 that the conventional interaction approach reduces the available flexural capacity at threaded joints as axial load increases. Rearranging equation 15 yields the maximum factored bending demand permitted by the interaction equation,

$$M_{u,\max} = \frac{1}{c_2}\, \phi_b M_n \left(1 - c_1 \frac{P_u}{\phi_a P_n}\right) \tag{18}$$

which explicitly shows that the allowable bending moment decreases monotonically with increasing axial load. As demonstrated by the experimental results presented in this study, this assumption is inconsistent with the observed behavior of threaded micropile joints under combined loading, where axial compression can delay gap opening and increase flexural capacity rather than reduce it.

The conventional interaction-based design approach is rooted in classical strength-of-materials concepts and does not explicitly account for the joint mechanics governing failure at threaded connections. As demonstrated by the experimental results presented in this study, failure at threaded micropile joints is typically governed by tensile-controlled mechanisms rather than by compressive yielding. As discussed in preceding sections, pre-compressive stresses—whether introduced through axial load or assembly-induced effects—delay joint seam separation and increase flexural capacity (see equation 9 to 13a). Neglecting the contribution of make-up torque for conservatism (i.e., assuming $T = 0$), the nominal flexural capacity of the joint may be expressed directly as a function of applied axial load,

$$M_n = M_j + k\frac{PS_g}{A_g} \tag{19}$$

Equation 19 is intended to represent failure modes governed by tensile stress development at the joint and does not capture failure governed by compressive yielding. As written, equation implies that flexural capacity increases indefinitely with increasing axial compression. In practice, however, sufficiently large axial loads may result in failure governed by yielding of the compression fibers. To account for this behavior, the joint capacity under compression-dominated conditions is approximated by combining equation 19 with the conventional interaction expression given by equation 18, resulting in,

$$M_{u,\max} = \frac{1}{c_2\phi_b}(M_j + P_u\frac{kS_g}{A_g})(1 - c_1\frac{P_u}{\phi_a P_n}) \tag{20}$$

Substituting $M_j = Zf_y$ and $P_n = 0.85A_sf_y$ into equation 20 yields the following reformulation,

$$M_{u,\max} = \frac{1}{c_2}\phi_b M_j(1 + \xi\frac{P_u}{P_n})(1 - c_1\frac{P_u}{\phi_a P_n}) \tag{21a}$$

where the modulation parameter $\xi$is defined as,

$$\xi = 0.85\,k\,\frac{A_sS_g}{A_gZ} \tag{21b}$$

The parameter ξ governs the degree to which axial compression enhances flexural capacity and depends on joint geometry through the terms A_s, A_g, and S_g, as well as on the assumed failure criterion through the plastic section parameter Z. When experimental data are available to characterize the pure bending behavior of threaded micropiles, as in the present study, Z may be taken as $Z = \beta Z_p$, resulting in $M_j = \beta Z_p f_y$. In the absence of test data, the proposed framework can readily incorporate the conventional 50%-Rule by assuming $Z = S_j$ and $M_j = S_j f_y$.

Simplified interaction diagrams derived from equation 18 and 21 are shown in Figure 24, where axial and bending demands are normalized as $P_u/(\phi_a P_n)$and $M_u/(\phi_b M_j)$, respectively. The failure envelope predicted by the proposed formulation (red curves) depends explicitly on the modulation parameter ξ and converges to the conventional interaction solution (black curve) as $\xi \to 0$.

At sufficiently high levels of axial compression, yielding of the casing in compression may occur prior to tensile failure of the threaded joint. Accordingly, the flexural capacity predicted by equation 21 must be bounded to ensure that it does not exceed the capacity of an intact casing section without reduced wall thickness. In particular, equation 21 may predict allowable factored bending moments greater than those associated with yielding of the continuous portions of casing, which is not physically admissible, as compression-controlled behavior would govern at these stress levels.

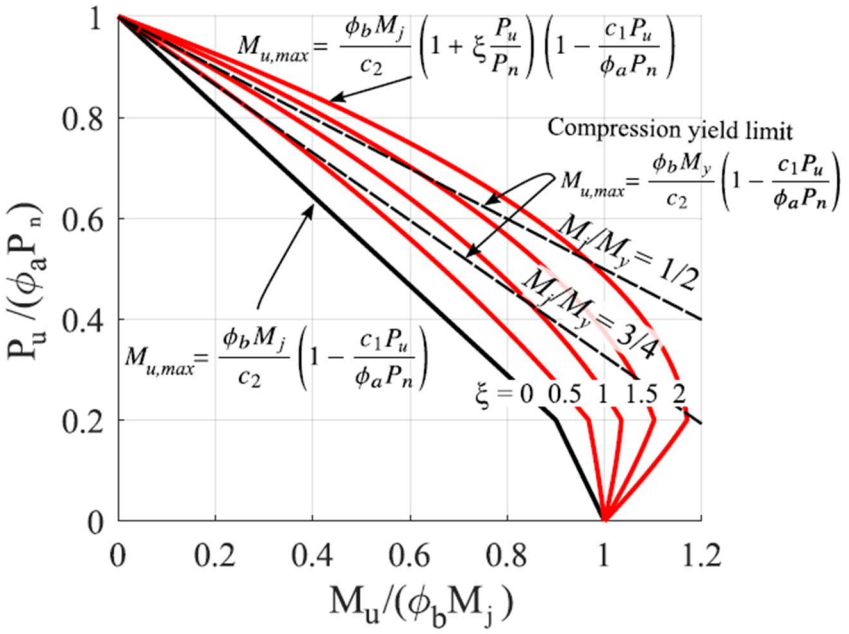

Figure 24. Combined loading interaction diagram for micropile threaded joints in axial compression. Limits for flexural yielding in compression are also shown for different assumed ratios of Mj/My.

The compression-controlled limit may be evaluated using the conventional interaction formulation given by equation 15 by setting $M_n = M_y$, where M_y is the yielding moment of the casing assuming full wall thickness and no joint reduction. To ensure physically consistent predictions, the maximum allowable factored bending moment is therefore taken as the lesser of the joint-controlled capacity predicted by,

$$M_{u,\max} = \text{Lesser of} \begin{cases} \text{Joint Capacity:} & \frac{1}{c_2}\,\phi_b M_j \left(1+\xi\frac{P_u}{P_n}\right)\left(1-c_1\frac{P_u}{\phi_a P_n}\right) \\ \text{Compression Limit:} & \frac{1}{c_2}\,\phi_b M_y \left(1-c_1\frac{P_u}{\phi_a P_n}\right) \end{cases} \tag{21}$$

The compression-controlled limit illustrated by the dashed lines in Figure 24, which correspond to representative ratios of joint flexural capacity to intact section capacity ($M_j/M_y = 0.5$ and 0.75). Previous experimental results have shown that the ratio M_j/M_y can range from approximately 0.5 to 0.9, depending on thread geometry and joint details (Montoya-Vargas et al., 2025a). Lower values of M_j/M_y imply that the beneficial effects of axial compression on joint flexural capacity may be realized over a wider range of axial loads, as shown by the dashed black envelopes in Figure 24. Conversely, as $M_j/M_y \to 1$, the joint capacity approaches that of an intact casing section, and the predicted response converges with the conventional interaction solution (solid black curve in Figure 24).

Using equation 21, the proposed failure envelopes are presented in Figure 25 for specimens with tapered thread walls using values of $\xi = 0.82$ and 0.96 (corresponding to thread lengths $L = 38$ and 57 mm, respectively, in Figure 25a), and for non-tapered wall threads with $\xi = 0.97$ (Figure

25b). These envelopes (red and blue curves) are compared directly with the conventional interaction approach (black curve). In typical design practice, nominal minimum guaranteed yield strength is assumed; for the specimens tested herein, this value was $f_y = 550$MPa and is shown by the continuous curves in Figure 25. However, coupon testing demonstrated that the actual yield strengths were significantly higher ($f_y = 700$ and 932 MPa), which are shown by the dashed curves. Yield strength directly influences both the joint-controlled capacity (Montoya-Vargas et al., 2025a) and the compression-controlled limit. Because designers generally do not know the actual yield strength, it is important to evaluate design recommendations using nominal properties while interpreting experimental performance—shown by open symbols in Figure 25—in the context of measured material strength.

As shown in Figure 25, the flexural capacities measured for the tested specimens exceed the threshold capacities predicted by the proposed combined-loading interaction envelopes, both with and without axial compression. For the range of axial loads considered in this study, the proposed methodology justifies flexural capacities that are approximately 20–60 % greater for joints with tapered thread walls (Figure 25a) and approximately 35 % greater for joints with non-tapered thread walls (Figure 25b) when compared with the conventional interaction approach (black dashed curves). These results demonstrate that the proposed framework provides an adequate—and generally conservative—representation of joint behavior for the moderate axial compressive loads examined herein.

It is noted, however, that combined loading tests were not performed at higher axial compression levels that would span a larger portion of the interaction envelope. This limitation was primarily due to constraints associated with the available testing equipment and the axial capacity of the center bar used to apply compressive loads. Nevertheless, the applied axial loads fall within the range of geotechnical axial capacities typically associated with micropiles of the size tested, as indicated by the shaded region in Figure 25. While these results support the applicability of the proposed interaction envelopes within practical design ranges, additional experimental validation at higher axial compression levels—particularly near upper-bound geotechnical capacity limits—would be valuable to further confirm their conservatism.

Axial tension loading was not considered in this study, although micropiles are frequently used in anchorage applications where tensile forces may be present. In contrast to axial compression, which was shown to augment flexural capacity by delaying joint separation, axial tension is expected to reduce the flexural capacity of threaded micropile connections. While the proposed framework would predict a reduction in flexural capacity under axial tension, its adequacy for such conditions has not been verified experimentally. Investigation of combined flexure and axial tension would require a distinct experimental configuration from that employed herein and represents an important area for future research, given the relevance of flexural performance at threaded joints to the broader micropile engineering community.

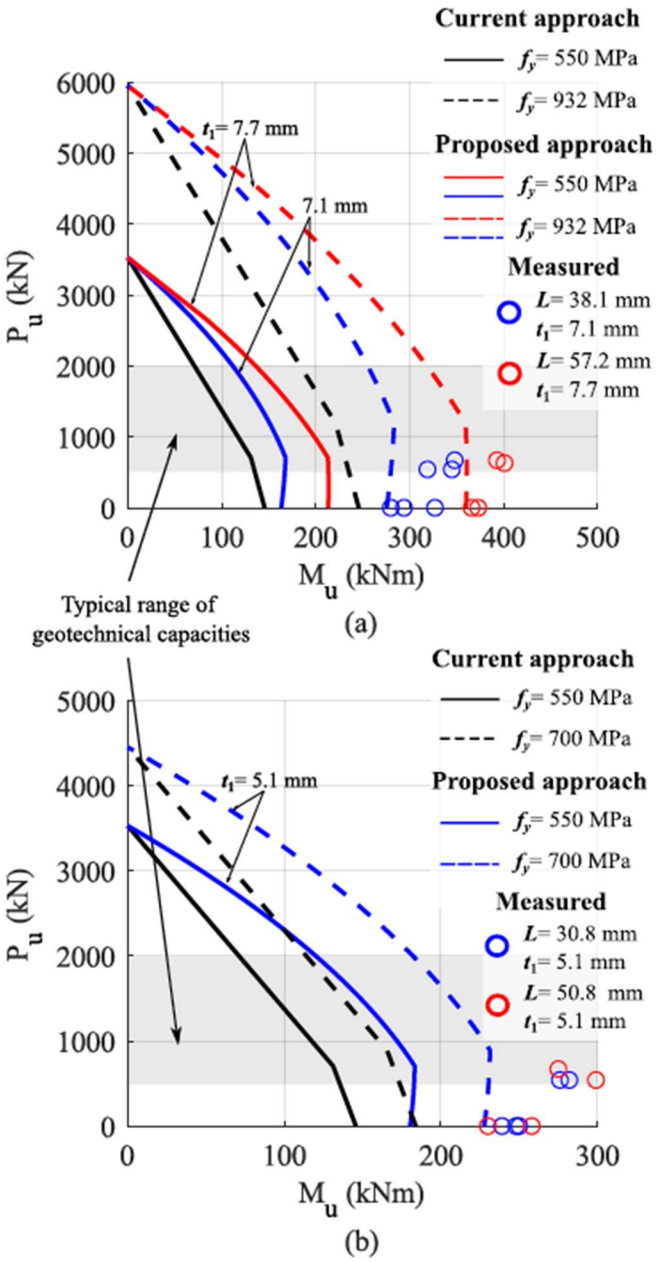

Figure 25. Current and proposed approach to construct combined loading interaction diagrams with nominal (f_y = 550 MPa) and actual (f_y = 932 or 700MPa) yield strengths for tested micropile specimens (solid vs. dashed lines) compared with observed flexural capacity at threaded joints for: a.) tapered thread walls and b.) non-tapered thread walls. Typical geotechnical design capacities are also indicated by the gray shaded regions for this micropile size.

Chapter 5: Summary and Conclusions

This study investigated the flexural behavior of threaded micropile connections under pure bending and combined axial compression and bending, with particular emphasis on joint-level kinematics and failure mechanisms that are not explicitly addressed in current design practice. A coordinated program of full-scale four-point bending tests, augmented with high-resolution digital image correlation, was used to directly observe deformation compatibility, strain localization, and failure processes at threaded joints. Building on these experimental observations, a mechanics-based analytical framework was developed to quantify the influence of axial compression on joint flexural capacity and to evaluate its implications for design.

Results from pure bending tests demonstrated that the flexural capacity of threaded micropile connections is governed by localized tensile-controlled joint kinematics rather than uniform section yielding. Two dominant failure modes—jump-out and rupture—were consistently observed, with the governing mode controlled by thread geometry, box-end wall thickness, thread engagement length, and casing diameter. These observations confirm that the commonly used 50%-Rule is generally conservative, but lacks a clear mechanical basis and does not adequately represent the kinematics that control joint strength.

Combined loading tests revealed an important and unconventional finding: axial compression can increase the flexural capacity of threaded micropile joints. Experimental results showed that applied axial compression delays joint seam separation by offsetting tensile stresses induced by bending, thereby increasing the moment required to initiate gap opening and subsequent failure. For the range of axial loads examined in this study—representative of typical geotechnical design loads for the tested micropile size—measured flexural capacities under combined loading exceeded pure bending capacities by an average of approximately 15%. This behavior contrasts with conventional axial–flexural interaction assumptions, which uniformly predict reduced bending capacity with increasing axial load.

The proposed analytical framework explicitly incorporates this behavior by relating flexural capacity to joint kinematics through the gap-opening moment. When applied to the experimental data, the framework provided accurate and generally conservative predictions of joint capacity across the casing sizes and thread geometries investigated. Relative to the conventional interaction approach currently used in design, the proposed method justified additional flexural capacity on the order of 20–60% for the joints evaluated in this study. These gains are consistent with the experimentally observed delay in joint separation and were achieved without exceeding the compressive capacity of the continuous casing section.

Importantly, the proposed interaction envelopes converge to conventional design solutions at higher axial load ratios, ensuring that compression-dominated failure modes are not unconservatively exceeded. For all tested specimens, observed failure moments remained below the compression-controlled limits of the intact casing, indicating that the proposed approach maintains appropriate bounds on flexural demand while more accurately reflecting joint mechanics. As such, the framework provides a physically consistent means of accounting for axial compression effects at threaded joints that are neglected in current practice.

Overall, this study demonstrates that flexural performance at threaded micropile connections is governed by joint-level deformation mechanisms and that axial compression can be beneficial rather than detrimental to flexural capacity within practical design ranges. By integrating experimental observations with a kinematics-based analytical model, the work provides both mechanistic insight and a rational basis for improving design approaches for micropiles subjected to combined loading.

Future research should extend combined loading experiments to higher axial compression levels approaching upper-bound geotechnical capacities, as well as to axial tension loading, which is expected to reduce flexural capacity and requires separate experimental validation. Additional testing across a broader range of thread geometries and casing sizes would further support refinement and generalization of the proposed design framework.

References

AASHTO. (2017). *LRFD bridge design specifications* (8th ed.). American Association of State Highway and Transportation Officials.

American Institute of Steel Construction (AISC). (2023). *Specification for Structural Steel Buildings (ANSI/AISC 360-22).* AISC, Chicago, IL.

Anderson, B. J., & Babalola, M. R. (2011). Lateral load testing micropiles to evaluate the impact of threaded joints and casing embedment on short micropiles in shallow rock. *DFI Journal: The Journal of the Deep Foundations Institute, 5*(2), 23–34.

Babalola, M. R. (2011). *Evaluation of the lateral response of micropiles via full-scale load testing* (Doctoral dissertation). The University of North Carolina at Charlotte.

Bailey, E. I. (1995). *7 inch pipe test*. Technical report prepared by Stress Engineering Services, Inc. for Malcolm Drilling Co., Inc.

Baragetti, S., & Terranova, A. (2004). Effects of over-torque on stress relief in conical threaded connections. *Journal of Mechanical Design*, *126*(2), 351–358.

Bruce, D. A., Cadden, A. W., & Sabatini, P. J. (2005). *Practical advice for foundation design—Micropiles for structural support*. Technical report.

Cerfontaine, B., White, D., Kwa, K., Gourvenec, S., Knappett, J., & Brown, M. (2023). Anchor geotechnics for floating offshore wind: Current technologies and future innovations. *Ocean Engineering, 279*, 114327. https://doi.org/10.1016/j.oceaneng.2023.114327

Clinedinst, W. O. (1965). *Strength of threaded joints for steel pipe*. Technical report.

de la Fuente, P., & Zanuy, C. (2009). *Estudio experimental sobre el comportamiento estructural de uniones de micropilotes* (Experimental study on the structural behavior of micropile joints). Technical report, Asociación de Empresas de Tecnología del Suelo y del Subsuelo (AETESS).

Froster, D., Gomez, J., & Robinson, H. D. (2021). *Full-scale testing of micropile casing* (Technical report). Nucor Skyline, United States.

Grabon, W. A., Osetek, M., & Mathia, T. G. (2018). Friction of threaded fasteners. *Tribology International*, *118*, 408–420. https://doi.org/10.1016/j.triboint.2017.10.014

Matos, R. P., Pinto, P. L., Rebelo, C. S., Gervásio, H. S., & Veljkovic, M. (2016). Improved design of tubular wind tower foundations using steel micropiles. *Structure and Infrastructure Engineering, 12*(9), 1038–1050. https://doi.org/10.1080/15732479.2015.1076853

Montoya-Vargas, S., Gallant, A., & Davids, W. G. (2023). Flexural strength of micropile threaded connections. In *Proceedings of Geo-Congress 2022* (pp. 218–227).

Montoya-Vargas, S., Gallant, A., & Davids, W. G. (2024). Four-point bending test of micropile threaded connections. In *Proceedings of Geo-Congress 2024* (pp. 206–214).

Montoya-Vargas, S. (2025). *Flexural Strength of Micropile Threaded Connections* (Doctoral dissertation, University of Maine). University of Maine Digital Commons.

Montoya-Vargas, S., Gallant, A., Davids, W. G., & Berube, K. (2025a). Bending failure mechanisms and kinematics of micropile threaded connections. *Structures, 78*, 109223. https://doi.org/10.1016/j.istruc.2025.109223

Montoya-Vargas, S., Gallant, A., Davids, W. G., & Berube, K. (2025b). Strain data and deflections from full-scale four-point bending test of micropile threaded connections. *Data in Brief*, 112119. https://doi.org/10.1016/j.dib.2025.112119

Musselman, S. R., Long, J. H., Carroll, N., & Farr, S. (2007). Bending strength of threaded micropile connections. In *Proceedings of the 32nd Deep Foundations Institute Annual Conference*. Colorado Springs, CO.

Pétursson, H., Collin, P., Veljkovic, M., & Andersson, J. (2011). Monitoring of a Swedish integral abutment bridge. *Structural Engineering International, 21*(2), 175–180. https://doi.org/10.2749/101686611X12994961034291

Richards, T. D. (2005). *Report on 9.625-inch micropile casing thread bending tests*. Technical report, Nicholson Construction Co.

Sabatini, P. J., Tanyu, B., Armour, T., Groneck, P., & Keeley, J. (2005). *Micropile design and construction reference manual*. Federal Highway Administration.

Sun, S. W., Zhu, B. Z., & Wang, J. C. (2013). Design method for stabilization of earth slopes with micropiles. *Soils and Foundations, 53*(4), 487–497. https://doi.org/10.1016/j.sandf.2013.06.002

Thusyanthan, I., Manceau, S., & Klapper, J. (2021). Shaft friction of grouted piles in rock from new database of pile load tests. In *Proceedings of the 31st International Ocean and Polar Engineering Conference* (pp. 1326–1331). International Society of Offshore and Polar Engineers.

Xiang, B., Zhang, L. M., Zhou, L.-R., He, Y.-Y., & Zhu, L. (2015). Field lateral load tests on slope-stabilization grouted pipe pile groups. *Journal of Geotechnical and Geoenvironmental Engineering, 141*(4). https://doi.org/10.1061/(ASCE)GT.1943-5606.0001220

Yang, K., Albatal, A., Taylor, R., & Farouz, E. (2024). An innovative micropile support of excavation system to meet challenging site constraints. In *Proceedings of Geo-Structures 2024* (pp. 370–378). https://doi.org/10.1061/9780784485842.035

Zanuy, C., de la Fuente, P., & Pinilla, M. (2012). Bending strength of threaded connections for micropiles. *Journal of Constructional Steel Research, 78*, 68–78.

ZEISS. (2023). *ZEISS quality tech guide*. ZEISS GOM Metrology.

Transportation Infrastructure Durability Center
AT THE UNIVERSITY OF MAINE

35 Flagstaff Road
Orono, Maine 04469
tidc@maine.edu
207.581.4376

www.tidc-utc.org